

# A microstructural model for homogenization and cracking of piezoelectric polycrystals

Ivano Benedetti<sup>a,\*</sup>, Vincenzo Gulizzi<sup>a</sup>, Alberto Milazzo<sup>a</sup>

<sup>a</sup>*Department of Engineering, University of Palermo, Viale delle Scienze, Edificio 8, Palermo, 90128, Italy.*

---

## Abstract

An original three-dimensional generalised micro-electro-mechanical model for computational homogenization and analysis of degradation and micro-cracking of piezoelectric polycrystalline materials is proposed in this study. The model is developed starting from a generalised electro-mechanical boundary integral representation of the micro-structural problem for the individual bulk grains and a generalised cohesive formulation is employed for studying intergranular micro-damage initiation and evolution into intergranular micro-cracks. To capture the electro-mechanical coupling at the evolving damaging intergranular interfaces, standard mechanical cohesive laws are enriched with suitable electro-mechanical terms. The boundary integral formulation allows the expression of the microstructural piezo-electric boundary value problem in terms of generalised grain boundary and intergranular displacements and tractions only, which implies some definite modelling advantages, namely: *a)* the natural inclusion of the intergranular cohesive laws in the formulation; *b)* a meaningful simplification of the analysis pre-processing stage, i.e. input data and mesh preparation; *c)* the reduction of the number of degrees of freedom of the overall analysis with respect to other popular numerical methods. The developed formulation has been applied to the computation of the effective properties, i.e. material homogenization, of BaTiO<sub>3</sub> crystal aggregates and to the investigation of micro-cracking in PZT-4 ceramics, providing consistent results.

**Keywords:** Piezoelectric materials, Polycrystalline materials, Micro-mechanics, Computational homogenization, Micro-cracking, Boundary element method

---

---

\*Corresponding author

Email addresses: [ivano.benedetti@unipa.it](mailto:ivano.benedetti@unipa.it) (Ivano Benedetti), [vincenzo.gulizzi@unipa.it](mailto:vincenzo.gulizzi@unipa.it) (Vincenzo Gulizzi), [alberto.milazzo@unipa.it](mailto:alberto.milazzo@unipa.it) (Alberto Milazzo)

## 1. Introduction

Piezoelectric polymers and ceramics are an important class of multi-physics and multi-functional materials [1, 2]. Thanks to their inherent coupling between mechanical and electrical fields, they have found application in the manufacturing of transducers and micro-electro-mechanical systems (MEMS) for several engineering applications, including smart structures [3], structural health monitoring [4, 5, 6] and energy harvesting [7].

In the design of effective piezoelectric devices, it is important to understand and consider the processes leading to material damage initiation and evolution, up to failure. The understanding of such mechanisms is particularly relevant in the case of piezo-ceramics, due to their inherent brittleness [8, 9, 10], and in the design of multilayer devices, in which piezoelectric materials are often combined with metallic layers [11, 12, 13, 14, 15].

In recent years, thanks to the advancements and affordability of microscopy and high performance computing (HPC), much research has been devoted to the experimental characterisation and computational modelling of materials at the nano/micro-scales, with the aim of enhancing our understanding of the link between materials' micro-structure and properties [16]. Computational micro-mechanics [17, 18], based on experimental materials characterisation, provides the opportunity to assess the effects of micro-structural features, e.g. grains size and orientations in polycrystalline materials or fibre size and alignment in fibre reinforced composites, on damage and crack initiation mechanisms at the micro-scale and on the transition of damage/cracks to the macro-scale.

Several widely used approaches to the analysis of initiation and evolution of cracks in heterogeneous materials are based on the use of cohesive laws within a finite element framework. Cohesive laws are suitable for modelling failure processes and predicting cracks initiation at material interfaces. Different approaches have been proposed and used for a broad array of problems [19, 20, 21, 22, 23]. The cohesive zone approach has also been used for investigating crack nucleation and propagation in polycrystalline materials, in conjunction with different numerical schemes such as the finite element method (FEM) [24, 25, 26] or the boundary element method (BEM) [27, 28, 29, 30, 31]. A micro-structural cohesive finite element model has been recently employed for the study of micro-cracking in piezoelectric materials [32].

The BEM is today employed in many areas of science and engineering [33, 34, 35]. One of the reasons of its popularity is that it allows pre-processing simplification and computational savings in

terms of both storage memory and solution time in several applications, due to the fact that only the boundary of the analysed domain needs to be discretised, thus allowing a reduction in the number of degrees of freedom necessary for the numerical treatment of a given problem. This aspect may be appealing in computational micro-mechanics that, due to the inclusion of detailed morphological and constitutive descriptions, generally induces high computational costs. The BEM has been extensively employed for the analysis of problems involving piezoelectric solids, with or without cracks [36, 37, 38, 39, 40]. On the other hand, recently, the method has been effectively used for the study of polycrystalline materials micro-mechanics, both in the two-dimensional [41, 27, 42, 31] as well as three-dimensional case [43, 28, 30, 44, 45, 46, 47]. The application of the BEM for effective multi-scale modelling has been demonstrated in Refs.[48, 29]. However, no comprehensive three-dimensional boundary element model for the study of the micro-cracking in piezoelectric polycrystalline materials has been developed yet, which forms the subject of the present study.

In this work, a boundary integral framework is developed, implemented and applied to two different classes of problems involving piezoelectric materials: *a*) their computational homogenization, i.e. the computation of the effective properties of piezoelectric aggregates, starting from the features of the individual piezoelectric crystals; *b*) the analysis of microstructural damage evolution and crack nucleation, through the employment of suitable generalised cohesive laws.

The framework is developed with the aim of providing a tool useful for the analysis of piezoelectric devices and is built using several key items. The artificial polycrystalline morphologies are generated through Voronoi-Laguerre tessellations. The individual piezoelectric grains are modelled employing a generalised 3D boundary integral representation, which eventually results in a multi-region generalised BEM formulation for the overall aggregate. The interface between contiguous grains is represented using electro-mechanical cohesive laws embodying an irreversible damage parameter for modelling the progressive interface degradation. The micro-structural evolution is tracked through an incremental-iterative solution algorithm, based on a coefficients matrix whose elements are continuously updated according to the status of grain boundaries, considering the appropriate mechanical, electrical and piezoelectric conditions. The developed model was validated against results available in the literature.

The paper is organised as follows. The algorithms for the generation of the artificial morphologies are discussed in Section 2. Section 3 introduces the key items of the formulation, namely the generalised constitutive model for the piezo-electric grains, the piezo-electric boundary integral

equations and the generalised inter-granular model. The numerical discretisation strategy, within the framework of the boundary integral formulation, and the incremental/iterative solution strategy  
65 are discussed in Section 4. Several numerical tests, confirming the potential and effectiveness of the developed and implemented model, are eventually presented in Section 5, before some discussion in Section 6 and the conclusions of the study.

## 2. Morphology generation and meshing

To simulate the behaviour of piezoelectric aggregates, it is essential to have a suitable representation of their microstructure. In this study, aggregates of piezoelectric crystals with different  
70 crystallographic orientations in the 3D space are considered. The polycrystalline specimens are contained within the volume  $V$  bounded by the surface  $S = \partial V$  and they are modelled through a multi-region boundary element formulation [34], in which each different region represents an individual grain.

The considered microstructures are generated through Voronoi-Laguerre tessellations of the  
75 analysed domain  $V$  [49, 50, 51, 52, 53]. Such tessellations are mathematically defined space filling geometric subdivisions of the considered volume and are widely accepted as first-order approximations of real polycrystalline microstructures. Each Voronoi-Laguerre cell represents an individual grain  $g$  and, geometrically, it is a convex polyhedron with boundary  $S^g$  comprised of the union  
80 of *flat* convex polygonal faces  $F_n^g$ , with  $n = 1, \dots, N_f^g$  and  $N_f^g$  denoting the number of faces of  $g$ . The tessellations can be effectively built using open source software packages such as **Voro++** (<http://math.lbl.gov/voro++/>) [54] or **Neper** (<http://neper.sourceforge.net>) [50].

Such software packages are particularly effective for the tessellation of convex domains  $V$ . For the tessellation of more general non-convex domains, which can be useful for representing specific  
85 MEMS components (e.g. micro-gears, brackets or beams), they can be used within the context of more comprehensive techniques, similar to those used in Refs.[55, 47], which involve operations of seeds selection and mirroring with respect to the geometrical boundary of the non-convex domain to represent, with the aim of reproducing such a boundary through the tessellation itself, through the controlled placement of the tessellation seeds. For further details, the interested readers are  
90 refereed to Ref.[47].

Once a polycrystalline morphology of  $V$  is obtained, its mesh must be generated, to discretise the micro-mechanics equations. A specific feature of the proposed formulation, at least in the case

of linear elastic grains, is that only the boundary of the grains, and not their interior volume, must be meshed, which induces a reduction in the order of the solving system. This aspect, in conjunction with the fact that the grains faces  $F_n^g$  are a collection of convex flat polygons, allows a remarkable simplification of the pre-processing stage of the analysis. Meshing is performed according to the techniques developed in Ref.[30]: each polygonal face  $F_n^g$  is subdivided into a collection of non-overlapping triangular and quadrangular, continuous and semi-discontinuous elements. Semi-discontinuous elements are used in proximity of the edges of the grain faces to avoid the complexities induced, in the boundary element formulation, by the collocation of nodes on regions with a non unique definition of the surface normal vector, see e.g. [56, 57]. The mesh size is selected so that the average element length  $l_e$  is considerably smaller than the cohesive zone size  $L_{cz}$  employed at the intergranular interfaces [27, 28], which can be estimated in terms of the material fracture toughness and the interface strength [58, 25, 59]. Given the statistical nature of the micro-morphology and the generally high number of grains and intergranular interfaces, adopting an effective discretisation scheme is essential for the smooth solution of the numerical problem: an effective discretisation scheme is instrumental in both ensuring a reduced number of degrees of freedom and a suitable average quality of the obtained mesh.

Fig.(1) illustrates the different kinds of tessellations that can be generated and analysed in the discussed framework. Fig.(2a) shows an individual grain generated by the adopted tessellation methodology: the grain has flat polygonal faces over which local reference systems are adopted. Fig.(2b) exemplifies the boundary elements and nodes induced by the adopted meshing strategy.

### 3. Boundary element modelling of piezoelectric polycrystalline materials

In this study, the homogenization and analysis of inter-granular damage and micro-cracking in piezoelectric polycrystalline microstructures are considered. The problem is tackled by employing a boundary integral formulation whose key items are: *a*) a suitable constitutive framework for the bulk piezoelectric grains; *b*) a set of boundary integral equations representing the electro-mechanical behaviour of the individual grains in terms of generalised grain boundary quantities; *c*) a suitable interface model able to capture damage nucleation, evolution, coalescence and failure at the inter-granular regions. In this Section, such key items are described, while the numerical discretisation and non-linear solution strategies are discussed in Section 4.

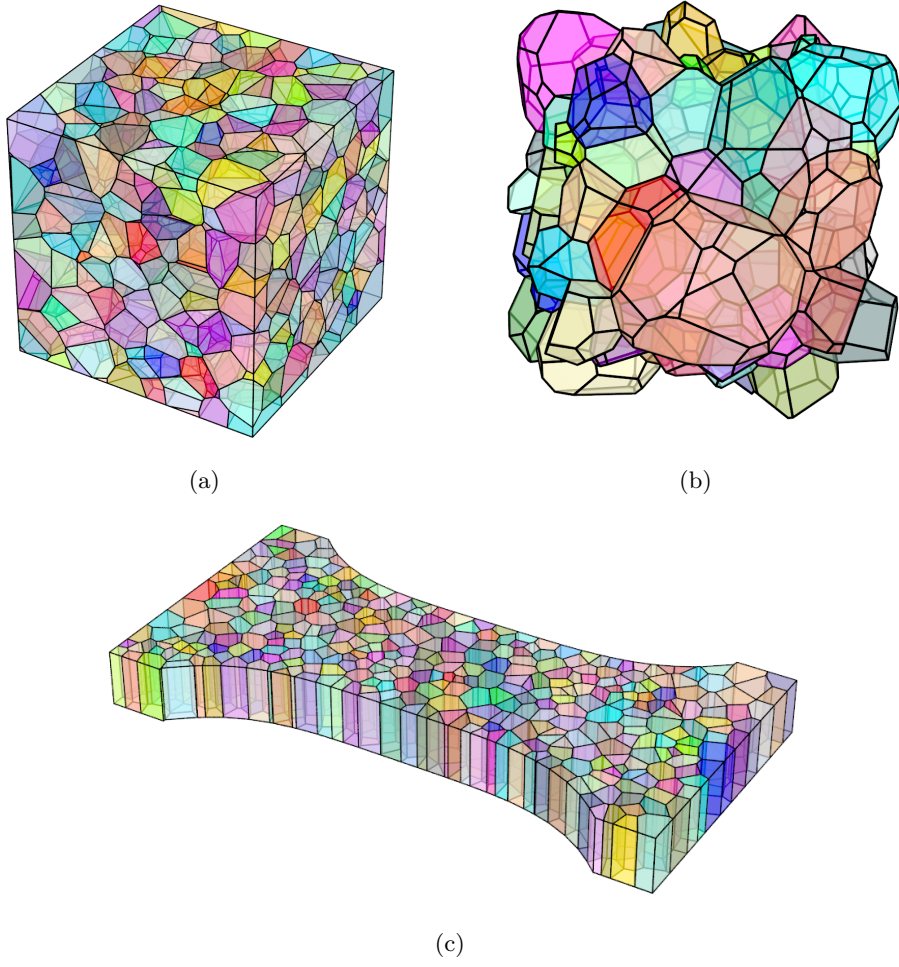


Figure 1: Different kinds of morphology can be generated and analysed within the proposed framework: *a*) example prismatic non-periodic 1000-grain tessellation; *b*) example non-prismatic periodic 100-grain tessellation, see Ref.[30]; *c*) tessellation of a non-convex domain: either 2D columnar or fully 3D morphologies can be generated, see Refs.[55, 47].

### 3.1. Piezoelectric materials modelling

The constitutive relations for linear piezoelectric materials can be written

$$\begin{aligned}
 \sigma_{ij} &= c_{ijkl} \gamma_{kl} - e_{kij} E_k \\
 D_i &= e_{ikl} \gamma_{kl} + \kappa_{ij} E_j
 \end{aligned} \tag{1}$$

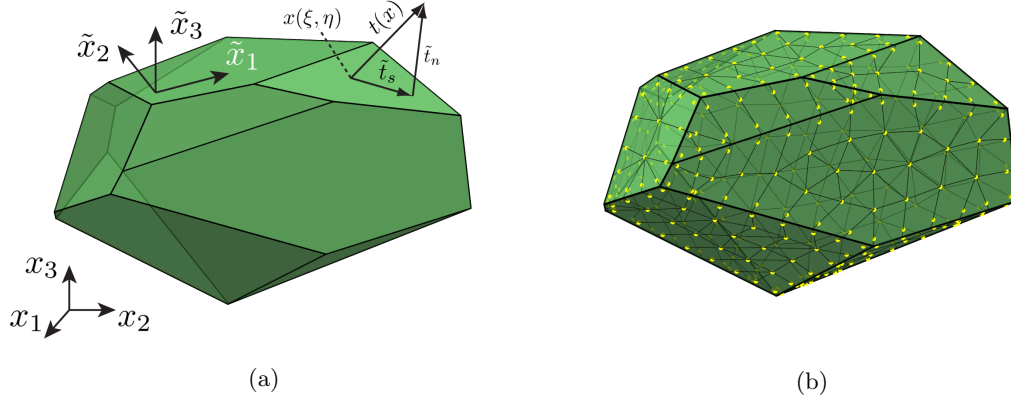


Figure 2: Morphology generation and meshing: *a)* an individual grain is a convex polyhedron with convex polygonal flat faces; face-local reference systems  $\tilde{x}_1\tilde{x}_2\tilde{x}_3$  are attached to *each* face and differ from the global reference system  $x_1x_2x_3$ ; the tractions  $\mathbf{t}(\xi, \eta)$  acting on the points of the faces can be conveniently decomposed into local normal  $\tilde{t}_n$  and tangential  $\tilde{t}_s$  components; *b)* meshing of the grain surface into non overlapping triangular and quadrangular elements; the collocation nodes are also highlighted. See Ref.[30] for further details about the meshing procedure.

where  $i, j = 1, 2, 3$ ,  $\sigma_{ij}$  and  $\gamma_{kl}$  are components of the second order stress and strain tensors,  $D_i$  and  $E_i$  are components of the electric displacement and electric field vectors,  $c_{ijkl}$  are components  
125 of the fourth order stiffness tensor,  $\kappa_{ij}$  are components of the second order dielectric tensor and  $e_{ijk}$  are components of the third order piezo-electric tensor. In the subsequent sections, when no confusion can be induced, we will simply refer to strains, stresses or other fields instead of strain, stress or other fields *components*, to make the text smoother.

The strains  $\gamma_{ij}$  and the electric field  $E_i$  are linked with the mechanical displacements  $u_i$  and the electric potential  $\phi$  by the relations

$$\gamma_{ij} = \frac{1}{2} (u_{i,j} + u_{j,i}), \quad E_i = -\phi_{,i}, \quad (2)$$

where, as customary, the comma in the subscripts denotes differentiation with respect to the coordinate identified by subsequent subscript.  
130

The mechanical stresses  $\sigma_{ij}$  and the electric displacement  $D_i$  fulfil the indefinite equilibrium equations and the Gauss' law of electrostatics respectively, that, in absence of body forces and free electric charges, are written

$$\sigma_{ij,j} = 0, \quad D_{i,i} = 0, \quad (3)$$

where repeated subscripts imply the Einstein's summation convention.

For the solution of the piezoelectric problem, the indefinite equations (3), the constitutive equations (1) and the compatibility equations (2) must be complemented by the mechanical and electrical boundary conditions

$$\begin{cases} u_i = \bar{u}_i & \text{on } S_u \\ t_i = \sigma_{ij}n_j = \bar{t}_i & \text{on } S_t \end{cases} \quad \begin{cases} \phi = \bar{\phi} & \text{on } S_\phi \\ \omega = -D_i n_i = \bar{\omega} & \text{on } S_D \end{cases} \quad (4)$$

where:  $S_u$ ,  $S_t$ ,  $S_\phi$  and  $S_\omega$  are regions of the external surface  $S$  over which the field identified by the subscript is known and such that  $S_u \cap S_t \equiv S_\phi \cap S_\omega \equiv \emptyset$  and  $S_u \cup S_t \equiv S_\phi \cup S_\omega \equiv S = \partial V$ ;  $n_i$  are the components of the unit outward normal;  $\omega$  denotes free/apparent electric charge surface density and the over-bar denotes known values.

The form of Eqs.(1-3) suggests the definition of *generalised* piezoelectric quantities. In particular, the components of *generalised piezoelectric displacements*  $U_i$  and *tractions*  $T_i$  are defined by

$$U_i = \begin{cases} u_i, & i \leq 3 \\ \phi, & i = 4 \end{cases}, \quad T_i = \begin{cases} t_i, & i \leq 3 \\ \omega, & i = 4 \end{cases}, \quad (5)$$

while the components of *generalised piezoelectric stresses*  $\Sigma_{ij}$  and *strains*  $\Gamma_{ij}$  are given by

$$\Sigma_{ij} = \begin{cases} \sigma_{ij}, & i \leq 3 \\ D_j, & i = 4 \end{cases}, \quad \Gamma_{ij} = \begin{cases} \gamma_{ij}, & i \leq 3 \\ -E_j, & i = 4 \end{cases}. \quad (6)$$

The definition of generalised displacements and tractions is the basis for the boundary integral formulation of the piezoelectric problem in the next Section.

### 3.2. Piezoelectric boundary integral equations

For each grain  $g$  of the aggregate the *generalised displacements boundary integral equations* can be written, in absence of body forces and free electric charge density, as

$$c_{ij}^g(\mathbf{x}) U_j^g(\mathbf{x}) + \int_{S^g} \hat{T}_{ij}^g(\mathbf{x}, \mathbf{y}) U_j^g(\mathbf{y}) dS(\mathbf{y}) = \int_{S^g} \hat{U}_{ij}^g(\mathbf{x}, \mathbf{y}) T_j^g(\mathbf{y}) dS(\mathbf{y}) \quad i, j = 1, \dots, 4 \quad (7)$$

where  $g = 1, \dots, N_g$  identifies the considered grain, bounded by the surface  $S^g$ ,  $\mathbf{x}, \mathbf{y} \in S^g$  denote the boundary collocation and integration points respectively,  $U_j^g$  and  $T_j^g$  are components of the generalised displacements and tractions defined in Eq.(5),  $c_{ij}^g$  are constants stemming from the limiting boundary collocation process [33, 34] and  $\hat{U}_{ij}^g$  and  $\hat{T}_{ij}^g$  are components of the generalised three-dimensional fundamental solutions, see Appendix A. In Eqs.(7),  $S^g = S_e^g \cup S_c^g$  is the boundary



of the  $g$ -th grain, which is given by the union of *external* regions  $S_e^g$ , over which boundary conditions  
 145 may generally be applied, and *contact* regions  $S_c^g$ , over which suitable inter-granular interface  
 conditions, must be enforced.

In Eqs.(7), the mechanical components of boundary displacements and tractions are expressed  
 in a unique and well defined reference system: for a given grain, a natural choice may be the  
 material reference system, identified by the material principal directions; a different choice may be  
 150 the selection of a unique *global* reference system for all the grains of the aggregate. In this work,  
 following Refs.[27, 43, 28], a different choice is made: with the aim of simplifying the expression of  
 the intergranular conditions, the mechanical boundary displacements and tractions are expressed  
 with respect to *local* face-by-face boundary reference systems that allow to highlight *normal* and  
*tangential* components and keep changing as the integration point span the boundary  $S^g$ , as shown  
 155 in Fig.(2b). The interested reader is referred to Refs.[27, 43, 28] for further details. This choice has  
 an apparent effect on the expression of the mechanical fields, i.e. displacements and tractions, but  
 it is also reflected in the expression of the normal components of the electric displacement vector at  
 an interface between two grains, which is to be considered when writing the electric intergranular  
 conditions. In the next sections, quantities expressed in such face local reference systems will be  
 160 denoted with an over-tilde  $\tilde{\cdot}$ .

### 3.3. Generalised modelling of the inter-granular interfaces

The interface shared between two generic grains  $a$  and  $b$  is generally assumed initially pristine;  
 however, during the electro-mechanical loading process, irreversible damage can nucleate, evolve and  
 coalesce, eventually originating macro-cracks. This micro-damaging/cracking process is modelled  
 165 using different sets of equations, according to the current *pristine*, *damaged* or *cracked* status of  
 the interface region.

In this model, the initial pristine interface  $I^{ab}$  between  $a$  and  $b$  can be thought as a zero-  
 thickness surface; the generic geometric point  $\mathbf{x} \in I^{ab}$  is thus shared between the grains and it  
 is simultaneously coincident with the two *physically distinct* points  $\mathbf{x}^a \in S^a$  and  $\mathbf{x}^b \in S^b$ , which  
 170 identify an *interface pair*. In the following equations, the short notation  $\tilde{u}_i^g$  and  $\tilde{t}_i^g$  will be used to  
 denote  $\tilde{u}_i(\mathbf{x}^g)$  and  $\tilde{t}_i(\mathbf{x}^g)$ , i.e. the displacements and tractions associated with the generic physical  
 grain-boundary point  $\mathbf{x}^g \in S^g$ , i.e. belonging to the boundary of the grain  $g$ . Analogous short  
 notation will be employed for the electrical fields.

### 3.3.1. Pristine interface

For a pristine interface pair, the *generalised displacements continuity* and *generalised tractions equilibrium* equations read

$$\begin{cases} \delta \tilde{u}_i = -\tilde{u}_i^a - \tilde{u}_i^b = 0 \\ \delta \phi = +\phi^a - \phi^b = 0 \end{cases} \quad \text{and} \quad \begin{cases} \tilde{t}_i^a - \tilde{t}_i^b = 0 \\ \tilde{\omega}^a + \tilde{\omega}^b = 0 \end{cases}, \quad (8a,b)$$

175 with  $i = 1, 2, 3$ . Eqs.(8a) express both mechanical and electrical continuity, so that the two physical points  $\mathbf{x}^a$  and  $\mathbf{x}^b$  share the same spatial location and exhibit the same electrical potential. Eqs.(8b), on the other hand, express both mechanical and electrical equilibrium, which implies that the two grains exchange the same mechanical tractions  $\tilde{t}_i^a = \tilde{t}_i^b$  through the interface at the point  $\mathbf{x} \in I^{ab}$  and that no net free electric charge localises at the interface upon loading. It is worth stressing  
180 that  $\tilde{u}_i^a$ ,  $\tilde{t}_i^a$ ,  $\tilde{\omega}^a$  are expressed in *their own* reference system, see Fig.(2a), while  $\tilde{u}_i^b$ ,  $\tilde{t}_i^b$  and  $\tilde{\omega}^b$  are expressed in the *opposite* system, which motivates the signs in the interface conditions given above. Due to the different nature of the mechanical and electrical conditions, it is not possible to use a simple unique generalised expression, in terms of  $\tilde{U}_i^g$  and  $\tilde{T}_i^g$ , for expressing the continuity and equilibrium conditions so that the mechanical and electrical intergranular equations must be stated  
185 explicitly and independently.

As the considered inter-granular interface evolves and damages, Eqs.(8b), i.e. the generalised tractions equilibrium, always hold and they will not be reported anymore. On the other hand, Eqs.(8a) will be replaced by generalised traction-separation laws, when the interface is damaged, and by by generalised frictional contact laws, when the interface fails originating a micro-crack.

### 190 3.3.2. Damaged interface

Damage arises at an interface pair when the *mechanical effective traction*  $\tilde{t}_e$ , defined as follows, fulfils, for the first time in the loading history, the following threshold condition

$$\tilde{t}_e = \sqrt{\langle \tilde{t}_n \rangle^2 + \left( \frac{\alpha_2}{\alpha_1} \tilde{t}_s \right)^2} \geq T_{\max} \quad (9)$$

where  $T_{\max}$  is the *mechanical interface cohesive strength*,  $\tilde{t}_n$  and  $\tilde{t}_s$  are the normal and tangential mechanical traction components, respectively,  $\alpha_1$  and  $\alpha_2$  are cohesive parameters governing the relative weight of mode I and mode II fracture toughnesses [27, 28] and  $\langle \cdot \rangle$  denote the McCauley's brackets, defined by  $\langle x \rangle = (x + |x|)/2$ . It is worth stressing that Eq.(9) is a purely mechanical  
195 condition; however, in principle, it can be activated by general electro-mechanical loads.

As Eq.(9) is fulfilled, a generalised traction-separation law of the form

$$\tilde{T}_i^a = C_{ij}(d^*, \delta \tilde{u}_n, \delta \phi) \delta \tilde{U}_j \quad (10)$$

is introduced at the considered interface pair, where  $d^*$  is a parameter quantifying the accumulated irreversible damage (see below) and  $\delta \tilde{u}_n$  is the normal component of displacement jump at the considered interface pair. More explicitly, using a decomposition into normal and tangential quantities for the mechanical variables, the generalised cohesive law can be written as

$$\begin{bmatrix} \tilde{t}_n \\ \tilde{t}_s \\ \tilde{\omega} \end{bmatrix}_a = \begin{bmatrix} C_{nn}(d^*) & 0 & C_{n\phi}(d^*, \delta \tilde{u}_n, \delta \phi) \\ 0 & C_{ss}(d^*) & 0 \\ 0 & 0 & C_{\omega\phi}(d^*, \delta \tilde{u}_n) \end{bmatrix} \begin{bmatrix} \delta \tilde{u}_n \\ \delta \tilde{u}_s \\ \delta \phi \end{bmatrix}, \quad (11)$$

where the terms

$$C_{nn}(d^*) = \frac{T_{\max}}{\delta u_n^{\text{cr}}} \frac{1 - d^*}{d^*}, \quad C_{ss}(d^*) = \frac{\alpha_1 T_{\max}}{\delta u_s^{\text{cr}}} \frac{1 - d^*}{d^*} \quad (12)$$

account for the purely mechanical part of the traction-separation law, with  $\delta u_n^{\text{cr}}$  and  $\delta u_s^{\text{cr}}$  denoting the critical displacement jumps in opening and sliding mode respectively and  $d^*$  is defined by

$$d^* = \max_{\mathcal{H}_d} \{d\} \in [0, 1], \quad \text{with } d = \sqrt{\left\langle \frac{\delta \tilde{u}_n}{\delta u_n^{\text{cr}}} \right\rangle^2 + \alpha_2^2 \left( \frac{\delta \tilde{u}_s}{\delta u_s^{\text{cr}}} \right)^2}, \quad (13)$$

i.e. as the maximum value attained by the mechanical *effective displacement*  $d$  during the loading process  $\mathcal{H}_d$ . The definition of  $d^*$  entails the distinction between *loading*, *unloading* and *reloading* status for the selected interface pair: in loading  $d = d^*$  and  $\dot{d} > 0$ , so that the interface accumulates damage and the constitutive parameters in the traction-separation laws evolve; in unloading  $d \leq d^*$ ,  $\dot{d} < 0$  and  $\dot{d}^* = 0$ ; in reloading  $d < d^*$ ,  $\dot{d} > 0$  and  $\dot{d}^* = 0$ . In unloading and reloading the damage remains constants, so that the constitutive cohesive parameters do not change.

On the other hand, according to Ref.[32], a phenomenological expression for the terms  $C_{\omega\phi}$  and  $C_{n\phi}$  can be obtained by considering the damaging interfaces as parallel-plate capacitors, which yields

$$C_{\omega\phi}(d^*, \delta \tilde{u}_n) = \frac{\hat{\kappa}_{gb}(d^*)}{\delta \tilde{u}_n}, \quad C_{n\phi}(d^*, \delta \tilde{u}_n, \delta \phi) = \frac{\hat{\kappa}_{gb}(d^*)}{2} \frac{\delta \phi}{\delta \tilde{u}_n^2}, \quad (14)$$

where  $\hat{\kappa}_{gb}(d^*) = (1 - d^*) \kappa_{gb} + d^* \kappa_0$  is the grain boundary permittivity, evolving from a pristine value  $\kappa_{gb}$  to the permittivity of vacuum  $\kappa_0$ , as damage evolves from zero to failure ( $d^* = 1$ ). In a capacitor with infinite and parallel flat plates, containing a dielectric medium, the relationship  $\tilde{\omega}^a = C_{\omega\phi} \cdot \delta \phi$  expresses the link between the electric charge density  $\omega^a$  at the plates and the electric

potential difference  $\delta\phi$  between the plates themselves. On the other hand,  $t_n^a = C_{n\phi} \cdot \delta\phi$  expresses the mutual mechanical attraction between the plates.

Few considerations are worthwhile. First of all, it should be noted that Eqs.(11) hold in *opening* mode, i.e. when  $\delta\tilde{u}_n > 0$ . In *compression*, when  $\delta\tilde{u}_n = 0$  and  $\tilde{t}_n < 0$ , the first and third equations in Eqs.(11) should be replaced by

$$\delta\tilde{u}_n = 0, \quad \delta\phi = 0, \quad (15)$$

which must be implemented directly into the system. The iso-electricity condition  $\delta\phi = 0$  is equivalent to assuming the points of the considered interface pair in strict contact. This is different from what is proposed in Ref.[32], where a material parameter  $d_{gb}$ , accounting for the grain boundary thickness when  $\delta\tilde{u}_n = 0$ , is introduced to address potential singularities arising with non-zero grain-boundary potential jumps. On the other hand, the presence of an intergranular thickness  $d_{gb}$  can be easily accommodated within the proposed formulation. In this case, here and in Eqs.(8a), the iso-electricity condition should be replaced by

$$d_{gb} \cdot \tilde{\omega}^a = \kappa_{gb} \cdot \delta\phi, \quad (16)$$

while  $\delta\tilde{u}_n$  should be replaced by  $(d_{gb} + \delta\tilde{u}_n)$  in Eqs(14). In Eq.(16), it is assumed that the closure restores the grain-boundary permittivity to  $\kappa_{gb}$ .

210 Eventually, it is worth noting that Eqs.(14) correspond to assuming the intergranular interface as an *electrically semi-permeable* discontinuity evolving between the flat plates of an *infinite* capacitor, which remain parallel as the loading/damaging process progresses. In the literature about cracks in piezoelectric media, two opposite assumptions are generally identifiable [60]: the assumption of electrically impermeable cracks, found e.g. in Refs.[61, 62], and that of electrically permeable  
215 cracks, discussed e.g. in Refs.[63, 64]. Considering an evolving interface as a flat-plate capacitor corresponds, as a matter of fact, to the assumption of semi-permeable crack [65]. The validity and limitations of the above assumptions in modelling polycrystalline piezoelectric aggregates are discussed in Ref.[32]. Although the applicability of different electrical permeability conditions is the subject of numerous investigations [66, 60, 67], it is worth stressing that the present computational  
220 framework can accommodate different and general interface conditions.

### 3.3.3. Failed interface

As the condition  $d^* = 1$  is fulfilled, mechanical failure is triggered at the considered interface pair. The mechanical interaction between the grains is modelled resorting to the equations of frictional contact, modified to take into account the electrical interactions. Three different statuses are possible, depending on the condition that are met at the interface: *separation*, *contact-slip* and *contact-stick*.

In separation, the condition  $\delta \tilde{u}_n > 0$  is fulfilled and the following equations are implemented

$$\tilde{t}_n^a = \frac{\kappa_0}{2} \frac{\delta \phi^2}{\delta \tilde{u}_n^2}, \quad \tilde{t}_s^a = 0, \quad \tilde{\omega}^a \delta \tilde{u}_n = \kappa_0 \delta \phi, \quad (17)$$

which may be obtained from Eqs.(11) setting  $d^* = 1$ . Differently from the purely mechanical case, an electrostatic mutual attraction may persist, if  $\delta \phi \neq 0$ , also when the mechanical integrity of the intergranular interface is lost.

In contact-slip,  $|t_s| = \mu |t_n|$ , where  $\mu$  is the friction coefficient, the mechanical tangential traction  $\mathbf{t}_s^a$  and displacement jump  $\delta \mathbf{u}_s$  have the same direction and the following equations are implemented

$$\delta \tilde{u}_n = 0, \quad \tilde{t}_s^a + \mu \tilde{t}_n^a = 0, \quad \tilde{\omega}^a d_{gb} = \kappa_{gb} \delta \phi, \quad (18)$$

where, again, it is assumed that the closure restores the grain-boundary permittivity to  $\kappa_{gb}$  and the presence of a grain-boundary thickness is taken into account for generality.

In contact-stick,  $|t_s| < \mu |t_n|$  and the following equations are implemented

$$\delta \tilde{u}_n = 0, \quad \delta \dot{\tilde{u}}_s = 0, \quad \tilde{\omega}^a d_{gb} = \kappa_{gb} \delta \phi, \quad (19)$$

where the over-dot indicates the derivative with respect to the loading parameter. Further details about the implementation of the frictional contact conditions can be found in Ref.[28]: the above equations constitute a suitable generalisation for taking into account the presence of electrical effects at the intergranular interfaces.

## 4. Numerical discretisation and non-linear system solution

For the effective numerical treatment of the micro-structural piezoelectric problem, the boundary integral equations presented in Section 3.2 and the interface conditions discussed in Section 3.3 must be suitably implemented. The steps for discretising the equations and solving the resulting algebraic system are discussed here.

#### 4.1. Discretisation

For each piezo-electric crystal  $g$  within the micro-morphology, Eqs.(7) are used in the framework of the boundary element method [34, 33, 30], according to the following steps:

- The boundary of each grain  $g$  is subdivided into a set of non-overlapping triangular and quadrangular elements  $e$ ;
- The generalised piezoelectric displacements  $\tilde{U}_i^g$  and tractions  $\tilde{T}_i^g$  are expressed, over each element  $e$ , as

$$\tilde{U}_i^{ge} = N_k^e(\xi, \eta) \tilde{\Delta}_{ik}^e, \quad \tilde{T}_i^{ge} = N_k^e(\xi, \eta) \tilde{\Psi}_{ik}^e \quad (20)$$

where  $N_k^e(\xi, \eta)$  are suitable shape functions, defined in element-local 2D coordinates  $\{\xi, \eta\}$  and  $\tilde{\Delta}_{ik}^e$  and  $\tilde{\Psi}_{ik}^e$  are nodal values of generalised boundary displacements and tractions, expressed in face-local reference systems. In Eq.(20) the summation is implied only with respect to  $k = \{1, 2, \dots, M^e\}$ , where  $M^e$  is the number of nodes belonging to the element  $e$ ; the superscripts  $e$  and  $g$  are only used to identify the element and the grain, while the subscript  $i = 1, \dots, 4$  identifies the vector component of the considered field. After applying this procedure, a set of boundary elements and corresponding nodal points are associated to each grain;

- Eqs.(7) are then collocated at *each* of the  $M^g$  nodes of the considered crystal and *numerically integrated*, considering the above elemental approximation of the boundary fields [34].

After implementing the above discretisation scheme, a set of  $4 \times M^g$  equations is written for the  $g$ -th grain as

$$\tilde{\mathbf{H}}^g \cdot \tilde{\mathbf{\Delta}}^g = \tilde{\mathbf{G}}^g \cdot \tilde{\mathbf{\Psi}}^g, \quad (21)$$

where  $\tilde{\mathbf{\Delta}}^g$  and  $\tilde{\mathbf{\Psi}}^g$  collect the nodal values of generalised displacements and tractions of the  $M^g$  nodes belonging to the  $g$ -th grain,  $\tilde{\mathbf{H}}^g$  and  $\tilde{\mathbf{G}}^g$  are the matrices stemming from the numerical integration, in Eqs.(7), of the kernels components  $\hat{T}_{ij}^g$  and  $\hat{U}_{ij}^g$  multiplied by the relevant rotation matrices, shape function and Jacobian terms. In the numerical integration, care must be taken when integrating over *singular* elements, i.e. the elements containing the current collocation point. The interested readers are referred to Refs.[33, 34] for such specific aspects of the boundary element method.

The enforcement of active generalised boundary conditions (BCs) on the external walls of the aggregate leads, for *each* crystal, to the system

$$\mathbf{A}^g \cdot \mathbf{X}^g = \mathbf{B}^g \cdot \mathbf{Y}^g \quad (22)$$

260 where  $\mathbf{X}^g$  and  $\mathbf{Y}^g$  collect, respectively, the *unknown* and *known* nodal components of generalised grain-boundary displacements and tractions and  $\mathbf{A}^g$  and  $\mathbf{B}^g$  contain BCs-related combinations of columns of  $\tilde{\mathbf{H}}^g$  and  $\tilde{\mathbf{G}}^g$  [33, 34].

The equations for the overall polycrystalline aggregate are obtained coupling Eqs.(22), written for each grain, with the appropriate intergranular conditions, which leads to the following system

$$\begin{bmatrix} \mathbf{A} \\ \mathbf{I}(\mathbf{d}^*, \mathbf{X}) \end{bmatrix} \cdot \mathbf{X} = \begin{Bmatrix} \mathbf{B} \cdot \mathbf{Y}(\lambda) \\ \mathbf{0} \end{Bmatrix} \quad (23)$$

where

$$\mathbf{A} = \begin{bmatrix} \mathbf{A}^1 & \mathbf{0} & \dots & \mathbf{0} \\ \mathbf{0} & \mathbf{A}^2 & \dots & \mathbf{0} \\ \vdots & \vdots & \ddots & \vdots \\ \mathbf{0} & \mathbf{0} & \dots & \mathbf{A}^{N_g} \end{bmatrix}, \quad \mathbf{C} = \begin{bmatrix} \mathbf{C}^1 & \mathbf{0} & \dots & \mathbf{0} \\ \mathbf{0} & \mathbf{C}^2 & \dots & \mathbf{0} \\ \vdots & \vdots & \ddots & \vdots \\ \mathbf{0} & \mathbf{0} & \dots & \mathbf{C}^{N_g} \end{bmatrix},$$

being  $N_g$  the number of grains in the micro-morphology,  $\mathbf{X} = \{\mathbf{X}^1, \dots, \mathbf{X}^{N_g}\}$  the vector collecting the unknown degrees of freedom,  $\mathbf{Y} = \{\mathbf{Y}^1, \dots, \mathbf{Y}^{N_g}\}$  the vector collecting the prescribed nodal  
 265 values and  $\lambda$  a suitable load factor expressing the progressive loading of the aggregate. Eventually,  $\mathbf{I}(\mathbf{d}^*, \mathbf{X})$  implements the interface conditions that, in general, depend on the intergranular status, expressed by the vector  $\mathbf{d}^*$  collecting the damage values of all the interface pairs, and on the generalised displacement and traction fields, expressed by  $\mathbf{X}$ , as discussed in Section 3.3.

#### 4.2. Solution strategy

System (23) can be re-written in compact form as

$$\mathbf{M}(\mathbf{d}^*, \mathbf{X}) \cdot \mathbf{X} = \mathbf{Z}(\lambda), \quad (24)$$

270 which can be solved using an incremental/iterative algorithm for capturing the initiation, evolution, coalescence of intergranular damage and its growth into micro-cracking. The micro-structural evolution of the piezoelectric polycrystalline aggregate is triggered by the progressive increment of the external loads, generally expressed in terms of the load factor  $\lambda$ . The micro-evolution is tracked by

solving the boundary value problem for a discrete set of values  $\{\lambda_0, \lambda_1, \dots, \lambda_N\}$ . Once the solution  $\mathbf{X}_k$  corresponding to the load level  $\lambda_k$  is known, a new load increment  $\Delta\lambda_k$  is applied, so that the incremented load level  $\lambda_{k+1} = \lambda_k + \Delta\lambda_k$  is attained. The search of the new solution  $\mathbf{X}_{k+1}$  can then be performed using a Newton-Raphson algorithm for solving system (24).

Since matrix  $\mathbf{M}(\mathbf{d}^*, \mathbf{X})$  is sparse, the iterative solution of Eq.(24) is tackled in this work using the solver PARDISO (<http://www.pardiso-project.org/>). In the solution of Eq.(24), which stems from a boundary element collocation procedure, higher computational efficiency could be attained using Krylov iterative solvers in conjunction with special matrix representations, obtained for example using fast multipoles [68] or hierarchical matrices [69, 70, 71].

## 5. Numerical experiments

In this section, the developed formulation is employed to estimate the effective properties of polycrystalline aggregates of piezoelectric grains and to simulate their micro-cracking and the effect that the electromechanical coupling may have on the intergranular failure. All tests, except those involving the individual interface, have been performed on CINECA's Marconi's HPC infrastructure (<http://www.hpc.cineca.it/hardware/marconi>), on single nodes with 36 cores and 128 GB RAM.

### 5.1. Computational homogenization

The determination of the effective properties of piezoelectric polycrystalline materials has been tackled, using different techniques, in several literature works, see e.g. Refs. [72, 73, 74, 75, 76, 77].

In this section we estimate the effective properties of piezoelectric aggregates using computational homogenization algorithms based on the developed multi-field grain-boundary formulation. For the computation of the polycrystalline micro-fields, we employ non-prismatic periodic 3D unit cells, see Fig.(1), as discussed in Ref.[30]. The use of non-prismatic morphologies presents several advantages, e.g. minimisation of boundary layer artefacts and reduction of number of DoFs, over classical prismatic, generally cubic, unit cells.

Different types of boundary conditions can be enforced on the exterior of the polycrystalline morphology. In this work, periodic boundary conditions are considered as, in general, they provide faster convergence to material effective properties with respect to Dirichlet or Neumann boundary conditions. Considering two *opposite* and *coupled* external grain faces of the aggregate (note that,



being the aggregate non-prismatic, there are not external flat walls; however, couples of *opposite* conjugate grain faces can still be identified), one is assumed as the master face  $m$  while the other is denoted as the slave face  $s$ ; the mechanical and electric periodic boundary conditions are the implemented, in global coordinates, as follows

$$\begin{cases} u_i^s - u_i^m &= \langle \gamma_{ij} \rangle (x_j^s - x_j^m) \\ t_i^s + t_i^m &= 0 \end{cases}, \quad \begin{cases} \phi^s - \phi^m &= -\langle E_j \rangle (x_j^s - x_j^m) \\ \omega^s + \omega^m &= 0 \end{cases}, \quad (25)$$

where  $\langle \gamma_{ij} \rangle$  and  $\langle E_j \rangle$  are the prescribed components of macro- strain and electric field, respectively and the superscripts  $m$  and  $s$  denote field components of points belonging either to the master or slave face.

Once the aggregate boundary value problem is solved, the homogenized stress and electric displacement components can be estimated by using the relationships

$$\langle \sigma_{ij} \rangle = \frac{1}{V} \int_S t_i x_j dS, \quad \langle D_i \rangle = \frac{1}{V} \int_S \omega x_i dS, \quad (26)$$

which, being expressed in terms of integrals over the external surface  $S$  of the aggregate, can be conveniently computed within the context of the developed framework.

In the first set of tests we perform the computational homogenization of aggregates without texture, i.e. polycrystals in which the grains have random spatial orientation. In other words, the poling axes of the individual grains are not aligned along any specific direction and, for such a reason, it is expected that the aggregate does not exhibit any piezoelectric coupling, while it is possible to estimate the elastic and dielectric material constants. Fig.(3) reports the apparent values of the Young's modulus, shear modulus and relative dielectric constant versus the number of grains in unpoled aggregates of BaTiO<sub>3</sub> crystals. The material properties for BaTiO<sub>3</sub> single crystals are reported in Table 1. The individual volume averages are computed over sets of 100 realisations, each realisation being provided by a Laguerre-Voronoi tessellation obtained starting from randomly scattered seed points. Ensemble averages are then computed over the apparent properties corresponding to the individual realisation. It is possible to observe how the scattering of the apparent properties is reduced as the number of grains in the individual realisations grows, then approaching the effective values of the material properties. The homogenization results appear consistent with the values reported in Ref.[75].

Fig.(4) explores the role of poling on the effective properties of BaTiO<sub>3</sub> aggregates. Poling is enforced by constraining the angle  $\hat{\beta}$  formed between the material poling axis of the individual

Table 1: Material constants for barium titanate BaTiO<sub>3</sub> [75] and transversely isotropic lead zirconate titanate (PZT-4) [78].

Material property	Component	BaTiO <sub>3</sub>	PZT-4
<i>Elastic constants</i> [10 <sup>9</sup> N/m <sup>2</sup> ]	$c_{1111}, c_{2222}$	275.1	139.0
	$c_{3333}$	164.9	115.0
	$c_{1122}$	179.0	77.8
	$c_{1133}, c_{2233}$	151.6	74.3
	$c_{2323}, c_{1313}$	54.3	25.6
	$c_{1212}$	113.1	$(c_{1111} - c_{1122})/2$
<i>Piezoelectric constants</i> [C/m <sup>2</sup> ]	$e_{113}, e_{223}$	21.3	12.7
	$e_{333}$	3.7	15.1
	$e_{322}, e_{311}$	-2.7	-5.2
<i>Dielectric constants</i> [10 <sup>-9</sup> C/(V · m)]	$\kappa_{11}, \kappa_{22}$	16.9	6.5
	$\kappa_{33}$	0.9	5.6

crystals and a reference direction for the overall aggregate that, in the present work, is selected as the  $x_3$  aggregate direction. More specifically, the grains orientation is defined by the Euler angles  $(\hat{\alpha}, \hat{\beta}, \hat{\gamma})$ , according to the  $ZXZ$  convention (the symbol  $\hat{\cdot}$  is used here to avoid confusion between the Euler angles and the cohesive parameters  $\alpha_1$  and  $\alpha_2$ ):  $\hat{\alpha}$  and  $\hat{\gamma}$  represent rotations around the  $Z$  axis, which is assumed coincident with the grain poling axis, and are assumed to be uniformly distributed in the  $[0, 2\pi)$  interval; on the other hand, to account for the either unpoled, partially poled or fully poled aggregates, the angle  $\hat{\beta}$  is assumed to be distributed over the interval  $[0, \beta_{\max})$  according to the following probability density function

$$p(x) = \frac{\sin x}{2 \sin^2(\beta_{\max}/2)} \quad (27)$$

where  $\beta_{\max}$  denotes the maximum angle allowed between the poling axis and the  $x_3$  reference direction. It is clear that  $\beta_{\max} = \pi$  identifies an unpoled aggregate, whereas  $\beta_{\max} = 0$  defines a fully polarised state. The results reported in Fig.(4) correspond to  $\beta_{\max} = \pi$  and  $\beta_{\max} = \pi/4$  and highlight how the overall aggregate acquires piezoelectric properties as a consequence of the partial poling of the individual crystals. The computed material properties fall within the Voigt and Reuss

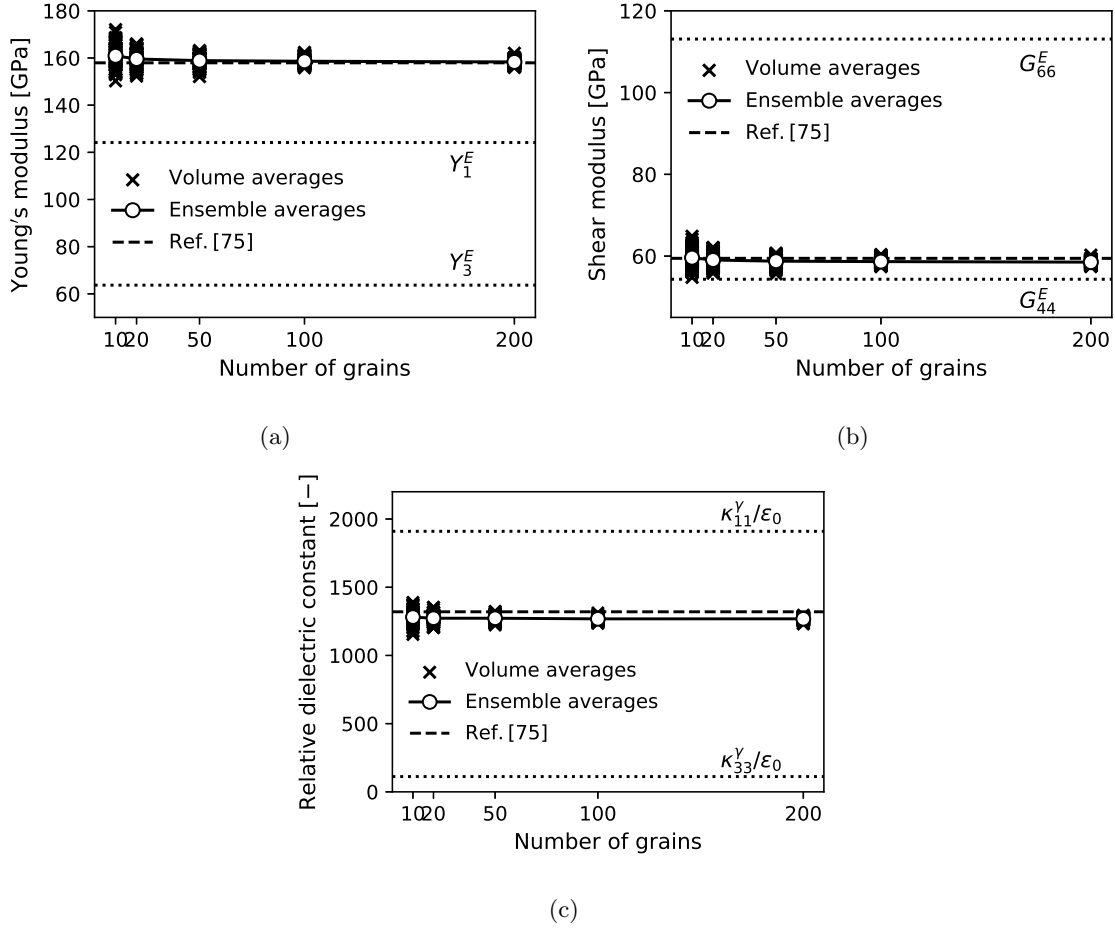


Figure 3: Apparent (a) Young's modulus, (b) Shear modulus and (c) relative dielectric constant as function of the number of grains for BaTiO<sub>3</sub> piezoelectric polycrystalline aggregates with isotropic grain orientation. Dotted lines denote the single crystal constants and  $\epsilon_0 = 8.854 \cdot 10^{-12} \text{ Fm}^{-1}$  is the vacuum permittivity constant. Constants' subscripts are given according to Voigt notation.

averages.

Fig.(5) reports the effective material properties of BaTiO<sub>3</sub> aggregates versus  $\beta_{\max}$ . The computed material properties always fall within the Voigt and Reuss averages. It is interesting to observe how isotropic macroscopic properties are retrieved when  $\beta_{\max} = \pi$ , which corresponds to unpoled aggregates.

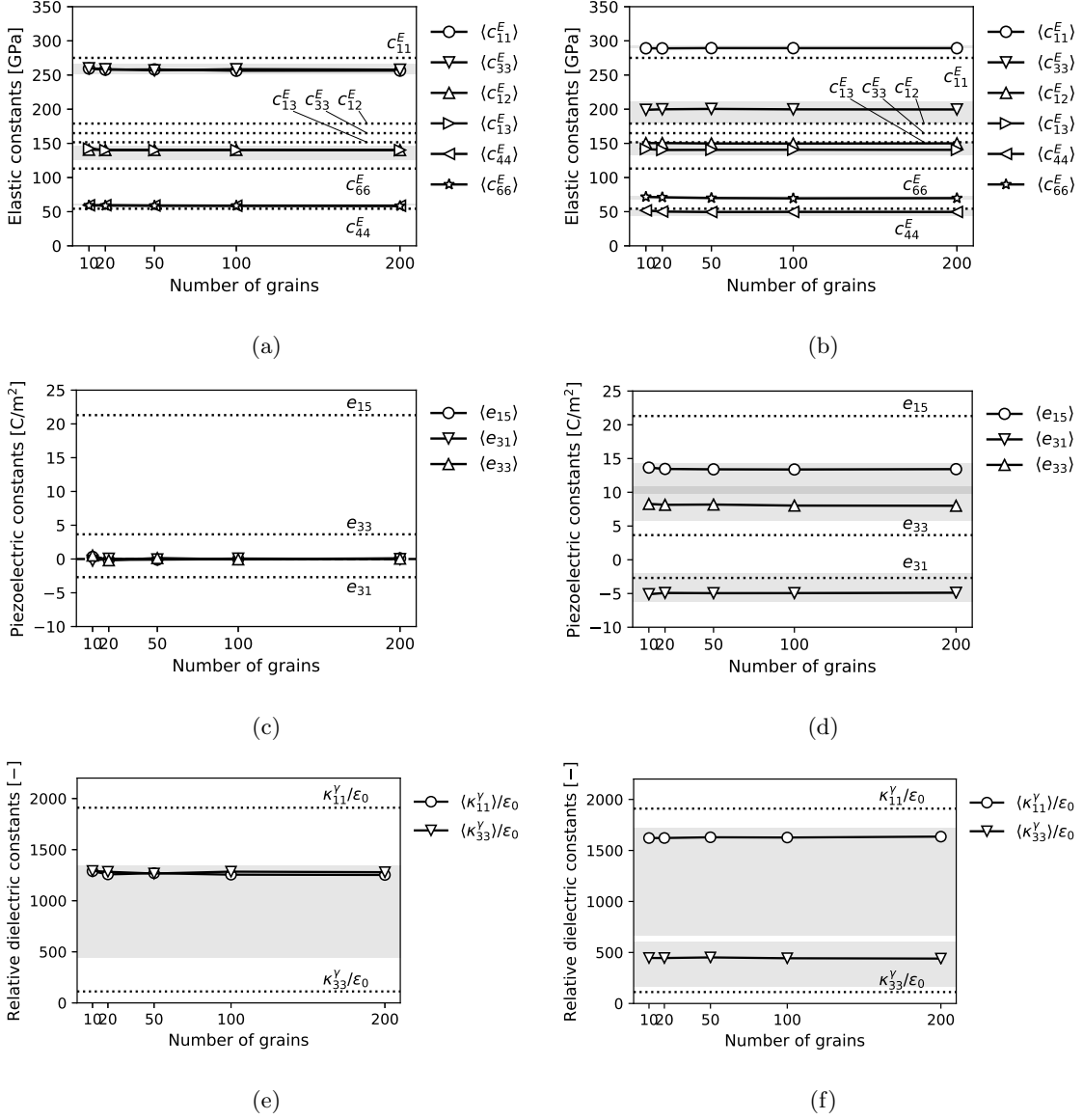


Figure 4: Apparent macroscopic constitutive properties of (a,c,e) unpoled ( $\beta_{\max} = \pi$ ) and (b,d,f) partially poled ( $\beta_{\max} = \pi/4$ ) as function of the number of grains for BaTiO<sub>3</sub> piezoelectric polycrystalline aggregates: (a,b) selected elastic constants, (c,d) selected piezoelectric constants, (e,f) selected dielectric constants. The grey regions around the shown constants denote the corresponding Voigt and Reuss averages. Dotted lines denote the single crystal constants and  $\epsilon_0 = 8.854 \cdot 10^{-12} \text{ Fm}^{-1}$  is the vacuum permittivity constant. Constants' subscripts are given according to Voigt notation.

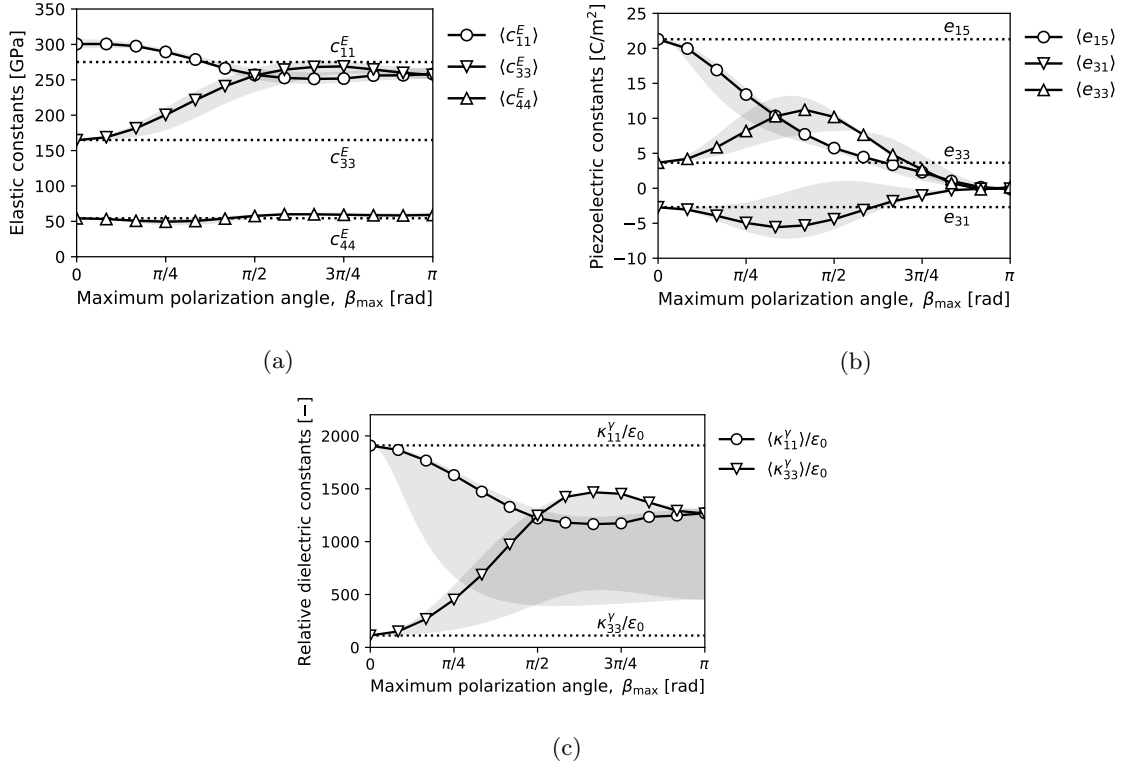


Figure 5: Apparent macroscopic constitutive properties of BaTiO<sub>3</sub> piezoelectric polycrystalline aggregates as a function of the maximum polarisation angle  $\beta_{\max}$ : (a) selected elastic constants, (b) selected piezoelectric constants, (c) selected dielectric constants. The grey regions around the shown constants denote the corresponding Voigt and Reuss averages as a function of  $\beta_{\max}$ . Dotted lines denote the single crystal constants and  $\epsilon_0 = 8.854 \cdot 10^{-12} \text{ Fm}^{-1}$  is the vacuum permittivity constant. Constants' subscripts are given according to Voigt notation.

## 5.2. Intergranular interface between piezoelectric grains

330 The simple system shown in Fig.(6a) is analysed here, to assess the behaviour of the cohesive interface between two piezoelectric domains and the effect of the piezoelectric coupling on the aggregate response. The system consists of two cubic PZT-4 crystals with edges of size  $l = 10 \mu\text{m}$  aligned with the reference axes, as represented by the arrows in the figure. The material properties for PZT-4, namely the constants  $C_{ijkl}$ ,  $e_{ijk}$  and  $\kappa_{ij}$ , are given in Table 1 and the poling vectors

335 of both domains are aligned with the  $x_3$  reference axis. The cohesive interface is identified by the material parameters  $(T_{max}, \delta u_n^{cr}, \delta u_s^{cr}, \alpha_1, \alpha_2, \kappa_{gb}, d_{gb})$  given in Table 2. The system is subjected to prescribed generalised displacements at the top and bottom surfaces; for the points belonging to

the lateral faces, the mechanical displacements along the normal  $n_i$ , the surface tangential traction components and the free electric charge are set to zero.

340 Fig.(6b) shows the effect on the curve of the homogenized stress component  $\langle \sigma_{33} \rangle$  versus a nominal measure of strain of the applied electric potential between the top and bottom faces of the two-crystal system: it is apparent how the piezoelectric effect may influence the macro-response, inducing either an increase or a decrease of the value of the homogenized response with respect to value found in the purely mechanical case. It is worth noting that, in this case, the effect  
345 is particularly evident because of the alignment of the poling axes of the two crystals with the external electric fields. As it will be shown next, in random or slightly textured polycrystals such effect may be less noticeable.

From the numerical point of view, it should be noted that, in this test, the external boundary conditions are applied in a non-proportional format: while the top face displacements evolve with  
350 the load factor  $\lambda$ , the electric potential on the top face is held constant during the mechanical loading, so that the right hand side Eq.(24) could be written as  $\mathbf{Z}(\lambda) = \lambda \mathbf{Z}_u + \bar{\phi} \mathbf{Z}_\phi$ . In general, the proposed formulation allows the enforcement of non-proportional loading: in this specific test the value of the initial potential had been previously assessed, so to verify that it would not induce initial damage at the interface between the grains and justify the use of an initial linear solution  
355 for  $\bar{u}_n = 0$ .

Table 2: Cohesive interface material parameters.  $\epsilon_0 = 8.854 \cdot 10^{-12} \text{ Fm}^{-1}$  is the vacuum permittivity constant.

$T_{max}$	$\delta u_n^{cr}$	$\delta u_s^{cr}$	$\alpha_1$	$\alpha_2$	$\kappa_{gb}$	$d_{gb}$
80 MPa	0.05 $\mu\text{m}$	0.1 $\mu\text{m}$	1	1	635 $\epsilon_0$	1 nm

### 5.3. Intergranular micro-cracking

The micro-cracking behaviour of piezoelectric polycrystalline aggregates is analysed here using  
360 the developed integral cohesive formulation.

Fig.(7) shows the homogenized component of stress  $\langle \sigma_{33} \rangle$  as a function of the applied macro-component of strain  $\langle \gamma_{33} \rangle$  for 100-grain PZT-4 aggregates simulated under the same boundary

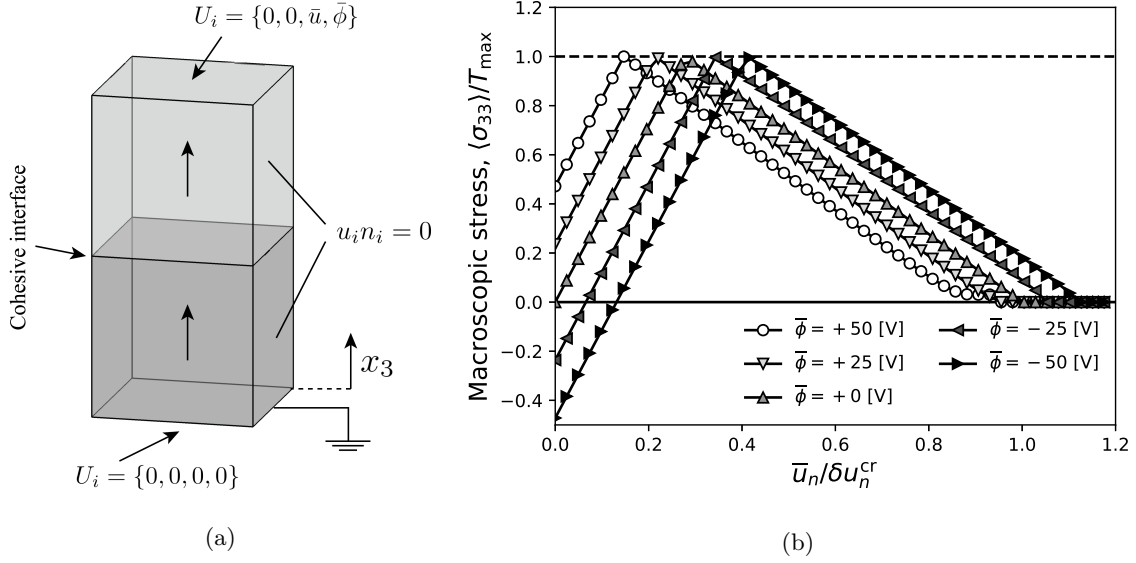


Figure 6: Effect of the piezoelectric coupling on the macroscopic stress for a simple two-crystal system: *a*) Geometry and boundary conditions for the analysed system (the grains are cubes with edge  $l$ ); *b*) homogenized stress component  $\langle \sigma_{33} \rangle$  at various levels of applied electric potential between the top and bottom face of the system.

conditions as those used for the two cubic grains in Fig.(6a). In this set of tests  $\beta_{\max} = \pi$ , so that there is no preferential grain poling direction, and the applied electric potential between the top and bottom surfaces of the aggregate is forced to zero, i.e.  $\bar{\phi} = 0$ . Fig.(7a) shows the response of five different morphologies  $M_I, \dots, M_V$  containing grains of average size  $d = 5 \mu\text{m}$  ( $d$  would be the diameter of a sphere with the grains average volume). It is possible to note how the five different morphologies exhibit almost the same macroscopic response so that, in this specific sense, morphologies with 100 grains can be considered representative of the material behaviour at the macro-scale. Fig.(7b) shows, under the same boundary conditions, the effect of the average grain size on the aggregate response: as the average grain size increases, more elastic energy is stored within the grains and then available to the micro-cracking process; as a consequence, if the cohesive parameters are kept unchanged, aggregates of larger grains appear more brittle with respect to aggregates of smaller ones.

The effect of the applied electric potential on the macroscopic stress-strain curve  $\langle \sigma_{33} \rangle$  versus  $\langle \gamma_{33} \rangle$  for different values of the maximum polarisation angle  $\beta_{\max}$  is investigated in Fig.(8), where the same 100-grain morphology is considered with four different distributions of the poling angle  $\hat{\beta}$ ,

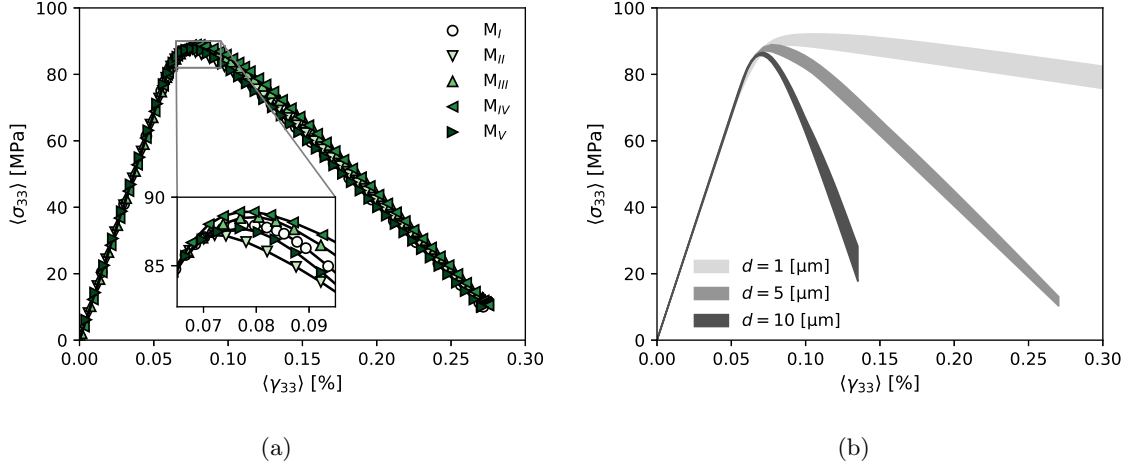


Figure 7: *a)* homogenized stress component  $\langle \sigma_{33} \rangle$  as a function of the applied strain  $\langle \gamma_{33} \rangle$  for five different realisations of a cubic 100-grain morphology with average grain size  $d = 5 \mu\text{m}$ . *b)* Effect of the average grain size  $d$  on the homogenized stress component  $\langle \sigma_{33} \rangle$  as a function of the applied strain  $\langle \gamma_{33} \rangle$ ; the displayed regions represent the envelopes of maximum and minimum values of the computed averaged stress component for five different random realisations of 100-grain morphologies for each considered value of the average grain size.

corresponding to the four selected values of  $\beta_{\text{max}}$ . It is apparent how the applied electric potential has little effect on macroscopic stress-strain curve of unpoled aggregates ( $\beta_{\text{max}} = \pi$ ), which do not exhibit macroscopic piezoelectric coupling, while the maximum effect is shown by the fully poled aggregates.

Fig.(9) investigates the effect of the applied electric potential on the link between the homogenized component  $\langle D_3 \rangle$  of the electric displacement and the applied strain  $\langle \gamma_{33} \rangle$ , for different values of the maximum polarisation angle  $\beta_{\text{max}}$ . It is interesting to observe that, for unpoled aggregates, the value of the macroscopic electric displacement depends almost only on the value of the external applied potential. This is due to the fact that, in such a case, the macroscopic effective piezoelectric constants vanish, so that the electric displacement components depend only on the applied electric field, see Eqs.(1). For partially or fully poled aggregates, on the contrary,  $\langle D_3 \rangle$  depends also on the value of the external applied strain  $\langle \gamma_{33} \rangle$ , as expected when the piezoelectric constants do not vanish.



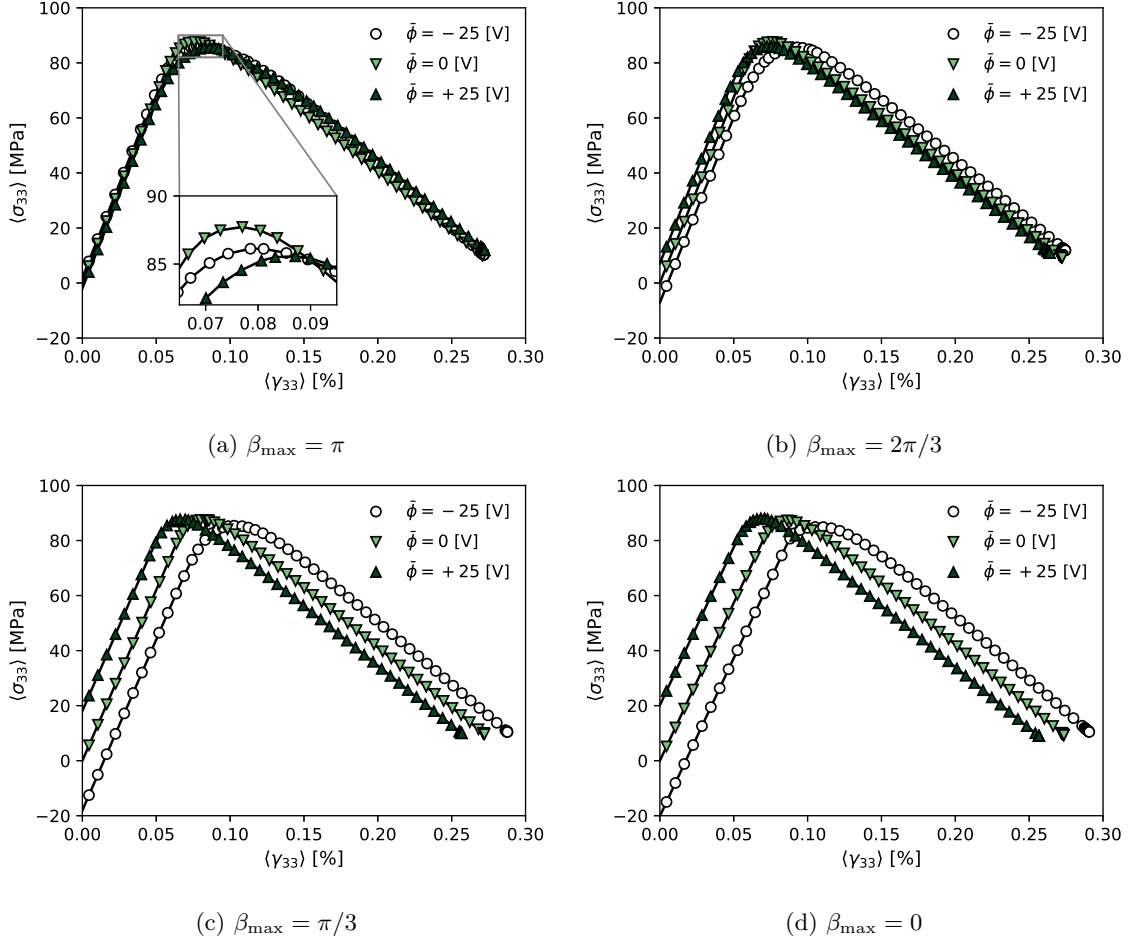


Figure 8: homogenized stress component  $\langle \sigma_{33} \rangle$  versus applied strain  $\langle \gamma_{33} \rangle$  for a cubic 100-grain morphology with average grain size  $d = 5 \mu\text{m}$  and different distributions of the poling angle  $\hat{\beta}$ . For each diagram, the three curves are obtained for three different level of applied electric potential between the top and bottom faces of the morphology. Figs.(a), (b), (c) and (d) are obtained by random distributions of  $\hat{\beta}$ , with the constraint on the maximum polarisation angle  $\beta_{\max} = \pi, 2\pi/3, \pi/3$  and 0, respectively.

## 6. Discussion

In this study an original boundary integral formulation for the analysis of intergranular failure of three-dimensional aggregates of piezoelectric grains has been developed, implemented, tested and applied to the homogenisation of piezoelectric polycrystalline materials and to the analysis of their micro-cracking. Although previous works have addressed the analysis of micro-cracking in piezo-

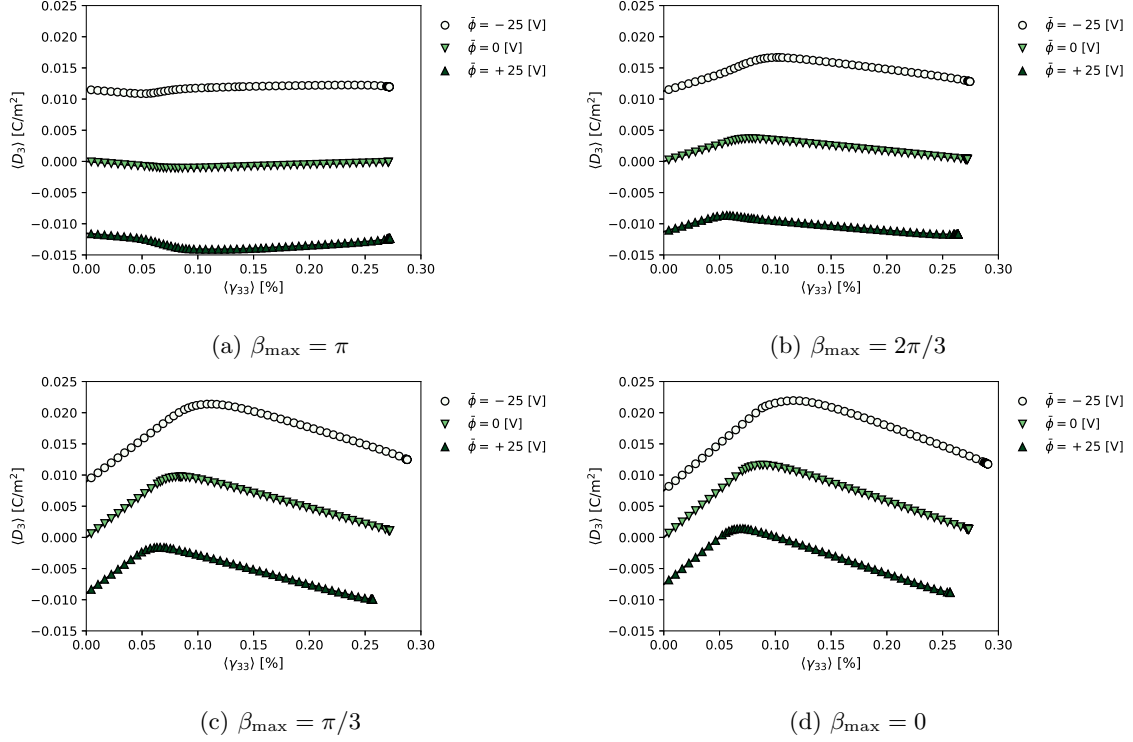


Figure 9: homogenized electric displacement component  $\langle D_3 \rangle$  as a function of the applied strain  $\langle \gamma_{33} \rangle$  of a cubic 100-grain morphology with average grain size  $d = 5 \mu\text{m}$ . For each figure, the three curves are obtained for three different level of applied electric potential between the top and bottom faces of the morphology. Figs.(a), (b), (c) and (d) are obtained by selecting the maximum polarisation angle equal to  $\beta_{\max} = \pi, 2\pi/3, \pi/3$  and 0, respectively.

electric aggregates, see e.g. Ref.[32], or have proposed multi-domain formulations for piezoelectric laminates [37], the one proposed here is the first fully three-dimensional boundary element model for the analysis of failure in polycrystalline piezoelectric materials.

Some specific aspects are worth mentioning here. In this study only intergranular damage and failure have been considered. The analysis of transgranular failure is certainly possible, as shown for example in Ref.[45], where a boundary integral formulation has been used for the analysis of inter- and transgranular failure of three-dimensional crystal aggregates. However, although conceptually very similar to the approach proposed in the present work, the consideration of transgranular cracks calls for partial re-meshing and the for a considerably more sophisticated implementation, beyond the scope of the proposed work. Assumed an available suitable characterisation of the material

parameters needed in the model, the extension to transgranular micro-cracking is certainly possible, but is left for future investigation.

As piezoelectric polycrystalline materials are often used in transducers subjected to cyclical loads [79], a line of further investigation could be addressed to the analysis of fatigue degradation in piezoelectric MEMS, following the approach suggested e.g. in Ref.[47].

In general, if coupled with suitable material characterisation at the microscale, the framework proposed here could be a valuable tool in the design of MEMS devices. Additionally, where the separation of scales holds, it could be used in the multiscale analysis of piezoelectric components, based on suitable computational homogenisation of representative volume elements.

## 7. Conclusions

An original framework for the computational homogenization and micro-cracking analysis of three-dimensional piezoelectric polycrystalline aggregates has been developed in this study. The developed tool is based on a boundary integral representation of the electro-mechanical problem for the individual grains of the aggregates and on the employment of generalised cohesive laws for the intergranular interfaces. The methodology has been implemented and tested for the computation of the effective properties of BaTiO<sub>3</sub> polycrystals, providing accurate estimates for various cases of unpoled, partially poled and poled aggregates. Subsequently, the micro-cracking behaviour of PZT-4 microstructures has been numerically studied, providing qualitatively consistent results. With suitable microstructural material input, the developed tool may offer valuable support in the design of MEMS devices.

## Acknowledgements

The authors acknowledge the support of CINECA's Italian Centre for Super Computing Applications and Innovation (SCAI) for access to and support in the use of their HPC infrastructure (<http://www.hpc.cineca.it>).

## Appendix A. Anisotropic Green's functions

The kernels  $\hat{U}_{ij}^g(\mathbf{x}, \mathbf{y})$  and  $\hat{T}_{ij}^g(\mathbf{x}, \mathbf{y})$  in Eq.(7) are given by

$$\hat{U}_{ij}^g(\mathbf{x}, \mathbf{y}) = G_{ij}^g(\mathbf{x}, \mathbf{y}), \quad \hat{T}_{ij}^g(\mathbf{x}, \mathbf{y}) = n_k(\mathbf{y}) C_{j k p q}^g \frac{\partial G_{ip}^g}{\partial y_q}(\mathbf{x}, \mathbf{y}) \quad (\text{A.1})$$

where  $i, j, p = 1, 2, 3, 4$  and  $k, q = 1, 2, 3$ ,  $\mathbf{n}(\mathbf{y}) = \{n_k(\mathbf{y})\}$  is the unit outward vector normal to the boundary at the point  $\mathbf{y}$  and  $C_{jkpq}^g$  is the *generalized* stiffness tensor defined as follows

$$C_{jkpq}^g = \begin{cases} c_{jkpq}^g, & j, p \leq 3 \\ e_{qjk}^g, & j \leq 3, p = 4 \\ e_{kpq}^g, & j = 4, p \leq 3 \\ -\kappa_{kq}^g, & j = p = 4 \end{cases}. \quad (\text{A.2})$$

In Eq.(A.1),  $G_{ij}^g(\mathbf{x}, \mathbf{y})$  are the 3D anisotropic Green's functions for the piezoelectric grain  $g$ , obtained as the solution of the differential system

$$C_{jkpq}^g \frac{\partial^2 G_{ip}^g}{\partial y_k \partial y_q}(\mathbf{x}, \mathbf{y}) + \delta_{ij} \cdot \delta(\mathbf{y} - \mathbf{x}) = 0 \quad (\text{A.3})$$

where  $\mathbf{x}$  and  $\mathbf{y}$  are the collocation and observation points, respectively,  $\delta_{ij}$  is the Kronecker delta and  $\delta(\mathbf{y} - \mathbf{x})$  is the Dirac delta function.

Using the Fourier transform with respect to  $\mathbf{y}$  to Eq.(A.3) and following in Ref.[80], the Green's functions  $G_{ij}^g(\mathbf{x}, \mathbf{y})$  and their derivatives can be obtained in terms of spherical harmonics as follows

$$\frac{\partial^{(I)} G_{ij}^g}{\partial r_1^{(\alpha_1)} \partial r_2^{(\alpha_2)} \partial r_3^{(\alpha_3)}}(\mathbf{r}) = \frac{1}{4\pi r^{I+1}} \sum_{\ell \in \mathcal{L}} P_\ell^I(0) \sum_{m=-\ell}^{\ell} \tilde{G}_{ij,(\alpha_1, \alpha_2, \alpha_3)}^{g, \ell m} Y^{\ell m}(\hat{\mathbf{r}}), \quad (\text{A.4})$$

where  $\mathbf{r} \equiv \mathbf{y} - \mathbf{x}$ ,  $r = \sqrt{r_k r_k}$ ,  $\hat{\mathbf{r}} = \mathbf{r}/r$ ;  $I = \alpha_1 + \alpha_2 + \alpha_3$  denotes the order of derivation and  $\mathcal{L}$  is the set of positive even (odd) integers when  $I$  is even (odd).  $P_\ell^I(0)$  is the  $\ell$ -th associated Legendre polynomials of degree  $I$  evaluated at 0 and  $Y^{\ell m}$  is the spherical harmonic of order  $\ell$  and degree  $m$ . The coefficients  $\tilde{G}_{ij,(\alpha_1, \alpha_2, \alpha_3)}^{g, \ell m}$  of the series are computed by means of the following integral over the unit sphere  $S_1$ :

$$\tilde{G}_{ij,(\alpha_1, \alpha_2, \alpha_3)}^{g, \ell m} = \int_{S_1} (\hat{\xi}_1)^{\alpha_1} (\hat{\xi}_2)^{\alpha_2} (\hat{\xi}_3)^{\alpha_3} \tilde{G}_{ij}^g(\hat{\xi}) \bar{Y}^{\ell m}(\hat{\xi}) dS(\hat{\xi}), \quad (\text{A.5})$$

being  $\tilde{G}_{ij}^g(\hat{\xi}) = (C_{ikjq}^g \xi_k \xi_q)^{-1}$  and  $\bar{Y}^{\ell m}$  the complex conjugate of  $Y^{\ell m}$ . The interested readers are referred to Ref.[80] for further details.

## References

- [1] K. S. Ramadan, D. Sameoto, S. Evoy, A review of piezoelectric polymers as functional materials for electromechanical transducers, *Smart Materials and Structures* 23 (3) (2014) 033001.

- [2] P. Panda, B. Sahoo, Pzt to lead free piezo ceramics: a review, *Ferroelectrics* 474 (1) (2015) 128–143.
- [3] C. Y. K. Chee, L. Tong, G. P. Steven, A review on the modelling of piezoelectric sensors and actuators incorporated in intelligent structures, *Journal of Intelligent Material Systems and Structures* 9 (1) (1998) 3–19. doi:10.1177/1045389X9800900101.
- [4] W. Staszewski, C. Boller, G. R. Tomlinson, *Health monitoring of aerospace structures: smart sensor technologies and signal processing*, John Wiley & Sons, 2004.
- [5] I. Benedetti, M. Aliabadi, A. Milazzo, A fast bem for the analysis of damaged structures with bonded piezoelectric sensors, *Computer Methods in Applied Mechanics and Engineering* 199 (9-12) (2010) 490–501.
- [6] F. Zou, I. Benedetti, M. Aliabadi, A boundary element model for structural health monitoring using piezoelectric transducers, *Smart Materials and Structures* 23 (1) (2013) 015022.
- [7] H. A. Sodano, D. J. Inman, G. Park, A review of power harvesting from vibration using piezoelectric materials, *Shock and Vibration Digest* 36 (3) (2004) 197–206.
- [8] Z. Suo, C.-M. Kuo, D. Barnett, J. Willis, Fracture mechanics for piezoelectric ceramics, *Journal of the Mechanics and Physics of Solids* 40 (4) (1992) 739–765.
- [9] Y. Pak, Linear electro-elastic fracture mechanics of piezoelectric materials, *International Journal of Fracture* 54 (1) (1992) 79–100.
- [10] T. Wang, X. Han, Fracture mechanics of piezoelectric materials, *International Journal of Fracture* 98 (1) (1999) 15–35.
- [11] A. Furuta, K. Uchino, Dynamic observation of crack propagation in piezoelectric multilayer actuators, *Journal of the American Ceramic Society* 76 (6) (1993) 1615–1617. doi:10.1111/j.1151-2916.1993.tb03950.x.  
URL <http://dx.doi.org/10.1111/j.1151-2916.1993.tb03950.x>
- [12] T. Hao, X. Gong, Z. Suo, Fracture mechanics for the design of ceramic multilayer actuators, *Journal of the Mechanics and Physics of Solids* 44 (1) (1996) 23 – 48. doi:http://dx.doi.

org/10.1016/0022-5096(95)00068-2.

URL <http://www.sciencedirect.com/science/article/pii/0022509695000682>

- [13] Y. Shindo, M. Yoshida, F. Narita, K. Horiguchi, Electroelastic field concentrations ahead  
465 of electrodes in multilayer piezoelectric actuators: experiment and finite element simulation,  
Journal of the Mechanics and Physics of Solids 52 (5) (2004) 1109 – 1124. doi:<http://dx.doi.org/10.1016/j.jmps.2003.09.017>.  
URL <http://www.sciencedirect.com/science/article/pii/S0022509603001601>
- [14] B. L. Wang, J. C. Han, An analytical model for electrode–ceramic interaction in multi-  
470 layer piezoelectric actuators, Acta Mechanica Sinica 23 (2) (2007) 199–208. doi:10.1007/  
s10409-007-0064-7.  
URL <http://dx.doi.org/10.1007/s10409-007-0064-7>
- [15] C. Häusler, H. Jelitto, P. Neumeister, H. Balke, G. A. Schneider, Interfacial fracture of piezo-  
electric multilayer actuators under mechanical and electrical loading, International Journal of  
475 Fracture 160 (1) (2009) 43–54. doi:10.1007/s10704-009-9408-6.  
URL <http://dx.doi.org/10.1007/s10704-009-9408-6>
- [16] S. Nemat-Nasser, M. Hori, Micromechanics: overall properties of heterogeneous materials,  
Vol. 37, Elsevier, 2013.
- [17] V. Kouznetsova, W. A. M. Brekelmans, F. P. T. Baaijens, An approach to micro-macro  
480 modeling of heterogeneous materials, Computational Mechanics 27 (1) (2001) 37–48. doi:  
10.1007/s004660000212.  
URL <http://dx.doi.org/10.1007/s004660000212>
- [18] T. I. Zohdi, P. Wriggers, An introduction to computational micromechanics, Springer Science  
& Business Media, 2008.
- [19] V. Tvergaard, Effect of fibre debonding in a whisker-reinforced metal, Materials Science and  
485 Engineering: A 125 (2) (1990) 203 – 213. doi:[http://dx.doi.org/10.1016/0921-5093\(90\)90170-8](http://dx.doi.org/10.1016/0921-5093(90)90170-8).  
URL <http://www.sciencedirect.com/science/article/pii/0921509390901708>

- [20] X. P. Xu, A. Needleman, Numerical simulations of dynamic interfacial crack growth allowing  
490 for crack growth away from the bond line, *International Journal of Fracture* 74 (3) (1996)  
253–275. doi:10.1007/BF00033830.  
URL <http://dx.doi.org/10.1007/BF00033830>
- [21] G. Camacho, M. Ortiz, Computational modelling of impact damage in brittle materials,  
*International Journal of Solids and Structures* 33 (20) (1996) 2899 – 2938. doi:[http://dx.doi.org/10.1016/0020-7683\(95\)00255-3](http://dx.doi.org/10.1016/0020-7683(95)00255-3).  
495 [http://dx.doi.org/10.1016/0020-7683\(95\)00255-3](http://dx.doi.org/10.1016/0020-7683(95)00255-3).  
URL <http://www.sciencedirect.com/science/article/pii/0020768395002553>
- [22] H. D. Espinosa, P. D. Zavattieri, S. K. Dwivedi, A finite deformation continuum  
discrete model for the description of fragmentation and damage in brittle materials, *Journal*  
*of the Mechanics and Physics of Solids* 46 (10) (1998) 1909 – 1942. doi:[http://dx.doi.org/](http://dx.doi.org/10.1016/S0022-5096(98)00027-1)  
500 [10.1016/S0022-5096\(98\)00027-1](http://dx.doi.org/10.1016/S0022-5096(98)00027-1).  
URL <http://www.sciencedirect.com/science/article/pii/S0022509698000271>
- [23] M. Ortiz, A. Pandolfi, Finite-deformation irreversible cohesive elements for three-dimensional  
crack-propagation analysis, *International Journal for Numerical Methods in Engineering* 44 (9)  
(1999) 1267–1282. doi:10.1002/(SICI)1097-0207(19990330)44:9<1267::AID-NME486>3.  
505 0.CO;2-7.  
URL [http://dx.doi.org/10.1002/\(SICI\)1097-0207\(19990330\)44:9<1267::AID-NME486>](http://dx.doi.org/10.1002/(SICI)1097-0207(19990330)44:9<1267::AID-NME486>3.0.CO;2-7)  
[3.0.CO;2-7](http://dx.doi.org/10.1002/(SICI)1097-0207(19990330)44:9<1267::AID-NME486>3.0.CO;2-7)
- [24] P. Zavattieri, P. Raghuram, H. Espinosa, A computational model of ceramic microstructures  
subjected to multi-axial dynamic loading, *Journal of the Mechanics and Physics of Solids* 49 (1)  
510 (2001) 27 – 68. doi:[http://dx.doi.org/10.1016/S0022-5096\(00\)00028-4](http://dx.doi.org/10.1016/S0022-5096(00)00028-4).  
URL <http://www.sciencedirect.com/science/article/pii/S0022509600000284>
- [25] H. D. Espinosa, P. D. Zavattieri, A grain level model for the study of failure initiation and  
evolution in polycrystalline brittle materials. part i: Theory and numerical implementation,  
*Mechanics of Materials* 35 (3) (2003) 333–364.
- [26] I. Simonovski, L. Cizelj, Cohesive zone modeling of intergranular cracking in polycrystalline  
515 aggregates, *Nuclear Engineering and Design* 283 (2015) 139–147.

- [27] G. Sfantos, M. Aliabadi, A boundary cohesive grain element formulation for modelling intergranular microfracture in polycrystalline brittle materials, *International journal for numerical methods in engineering* 69 (8) (2007) 1590–1626. doi:10.1002/nme.1831.
- 520 [28] I. Benedetti, M. Aliabadi, A three-dimensional cohesive-frictional grain-boundary micromechanical model for intergranular degradation and failure in polycrystalline materials, *Computer Methods in Applied Mechanics and Engineering* 265 (2013) 36–62. doi:10.1016/j.cma.2013.05.023.
- 525 [29] I. Benedetti, M. Aliabadi, Multiscale modeling of polycrystalline materials: A boundary element approach to material degradation and fracture, *Computer Methods in Applied Mechanics and Engineering* 289 (2015) 429 – 453. doi:http://dx.doi.org/10.1016/j.cma.2015.02.018.
- 530 [30] V. Gulizzi, A. Milazzo, I. Benedetti, An enhanced grain-boundary framework for computational homogenization and micro-cracking simulations of polycrystalline materials, *Computational Mechanics* 56 (4) (2015) 631–651. doi:10.1007/s00466-015-1192-8.
- [31] G. Geraci, M. Aliabadi, Micromechanical boundary element modelling of transgranular and intergranular cohesive cracking in polycrystalline materials, *Engineering Fracture Mechanics* 176 (2017) 351 – 374. doi:http://doi.org/10.1016/j.engfracmech.2017.03.016.  
URL http://www.sciencedirect.com/science/article/pii/S0013794417302825
- 535 [32] C. Verhoosel, M. Gutiérrez, Modelling inter- and transgranular fracture in piezoelectric polycrystals, *Engineering Fracture Mechanics* 76 (6) (2009) 742 – 760. doi:http://dx.doi.org/10.1016/j.engfracmech.2008.07.004.  
URL http://www.sciencedirect.com/science/article/pii/S0013794408001999
- [33] P. Banerjee, *The boundary element methods in engineering*, McGraw-Hill, 1994, (pp. 177–188).
- 540 [34] M. H. Aliabadi, *The boundary element method: applications in solids and structures.*, Vol. 2, John Wiley & Sons Ltd, England, 2002.
- [35] D. Beskos, G. Maier, *Boundary element advances in solid mechanics*, Vol. 440, Springer, 2014.
- [36] E. Pan, A bem analysis of fracture mechanics in 2d anisotropic piezoelectric solids, *Engineering Analysis with Boundary Elements* 23 (1) (1999) 67–76.



- [37] G. Daví, A. Milazzo, Multidomain boundary integral formulation for piezoelectric materials fracture mechanics, *International Journal of Solids and Structures* 38 (40) (2001) 7065–7078.
- [38] F. Garcia-Sanchez, A. Sáez, J. Dominguez, Anisotropic and piezoelectric materials fracture analysis by bem, *Computers & Structures* 83 (10) (2005) 804–820.
- [39] J. Sladek, V. Sladek, M. Wünsche, C. Zhang, Analysis of an interface crack between two dissimilar piezoelectric solids, *Engineering Fracture Mechanics* 89 (2012) 114–127.
- [40] J. Rungamornrat, W. Phongtinnaboot, A. Wijeyewickrema, Analysis of cracks in 3d piezoelectric media with various electrical boundary conditions, *International Journal of Fracture* 192 (2) (2015) 133–153.
- [41] P. Fotiu, R. Heuer, F. Ziegler, Bem analysis of grain boundary sliding in polycrystals, *Engineering Analysis with Boundary Elements* 15 (4) (1995) 349 – 358. doi:[http://dx.doi.org/10.1016/0955-7997\(95\)00037-0](http://dx.doi.org/10.1016/0955-7997(95)00037-0).  
URL <http://www.sciencedirect.com/science/article/pii/0955799795000370>
- [42] A. Galvis, P. Sollero, Boundary element analysis of crack problems in polycrystalline materials, *Procedia Materials Science* 3 (2014) 1928 – 1933. doi:<http://dx.doi.org/10.1016/j.mspro.2014.06.311>.  
URL <http://www.sciencedirect.com/science/article/pii/S2211812814003125>
- [43] I. Benedetti, M. Aliabadi, A three-dimensional grain boundary formulation for microstructural modeling of polycrystalline materials, *Computational Materials Science* 67 (2013) 249 – 260. doi:<http://dx.doi.org/10.1016/j.commatsci.2012.08.006>.  
URL <http://www.sciencedirect.com/science/article/pii/S0927025612004958>
- [44] I. Benedetti, V. Gulizzi, V. Mallardo, A grain boundary formulation for crystal plasticity, *International Journal of Plasticity* 83 (2016) 202–224. doi:[10.1016/j.ijplas.2016.04.010](http://dx.doi.org/10.1016/j.ijplas.2016.04.010).
- [45] V. Gulizzi, C. Rycroft, I. Benedetti, Modelling intergranular and transgranular micro-cracking in polycrystalline materials, *Computer Methods in Applied Mechanics and Engineering* 329 (2018) 168 – 194. doi:<https://doi.org/10.1016/j.cma.2017.10.005>.  
URL <http://www.sciencedirect.com/science/article/pii/S0045782517306746>

- [46] I. Benedetti, V. Gulizzi, A. Milazzo, Grain-boundary modelling of hydrogen assisted inter-granular stress corrosion cracking, *Mechanics of Materials* 117 (2018) 137 – 151. doi:<https://doi.org/10.1016/j.mechmat.2017.11.001>.  
575 URL <http://www.sciencedirect.com/science/article/pii/S0167663617305276>
- [47] I. Benedetti, V. Gulizzi, A grain-scale model for high-cycle fatigue degradation in polycrystalline materials, *International Journal of Fatigue* 116 (2018) 90 – 105. doi:<https://doi.org/10.1016/j.ijfatigue.2018.06.010>.  
URL <http://www.sciencedirect.com/science/article/pii/S0142112318302287>
- 580 [48] G. Sfantos, M. Aliabadi, Multi-scale boundary element modelling of material degradation and fracture, *Computer Methods in Applied Mechanics and Engineering* 196 (7) (2007) 1310–1329. doi:[10.1016/j.cma.2006.09.004](https://doi.org/10.1016/j.cma.2006.09.004).
- [49] F. Fritzen, T. Böhlke, E. Schnack, Periodic three-dimensional mesh generation for crystalline aggregates based on voronoi tessellations, *Computational Mechanics* 43 (5) (2009) 701–713.  
585 doi:[10.1007/s00466-008-0339-2](https://doi.org/10.1007/s00466-008-0339-2).  
URL <https://doi.org/10.1007/s00466-008-0339-2>
- [50] R. Quey, P. R. Dawson, F. Barbe, Large scale 3D random polycrystals for the finite element method: Generation, meshing and remeshing, *Computer Methods in Applied Mechanics and Engineering* 200 (2011) 1729–1745.
- 590 [51] C. Lautensack, Fitting three-dimensional laguerre tessellations to foam structures, *Journal of Applied Statistics* 35 (9) (2008) 985–995.
- [52] A. Lyckegaard, E. M. Lauridsen, W. Ludwig, R. W. Fonda, H. F. Poulsen, On the use of laguerre tessellations for representations of 3d grain structures, *Advanced Engineering Materials* 13 (3) (2011) 165–170. doi:[10.1002/adem.201000258](https://doi.org/10.1002/adem.201000258).  
595 URL <http://dx.doi.org/10.1002/adem.201000258>
- [53] R. Quey, L. Renversade, Optimal polyhedral description of 3d polycrystals: Method and application to statistical and synchrotron x-ray diffraction data, *Computer Methods in Applied Mechanics and Engineering* 330 (Supplement C) (2018) 308 – 333. doi:<https://doi.org/10.1016/j.cma.2017.10.029>.  
600 URL <http://www.sciencedirect.com/science/article/pii/S0045782517307028>

- [54] C. H. Rycroft, Voro++: A three-dimensional Voronoi cell library in C++, *Chaos* 19 (2009) 041111.
- [55] J. Bomidi, N. Weinzapfel, F. Sadeghi, Three-dimensional modelling of intergranular fatigue failure of fine grain polycrystalline metallic mems devices, *Fatigue & Fracture of Engineering Materials & Structures* 35 (11) (2012) 1007–1021.
- [56] L. Gray, E. Lutz, On the treatment of corners in the boundary element method, *Journal of Computational and Applied Mathematics* 32 (3) (1990) 369 – 386. doi:[https://doi.org/10.1016/0377-0427\(90\)90043-Y](https://doi.org/10.1016/0377-0427(90)90043-Y).  
URL <http://www.sciencedirect.com/science/article/pii/037704279090043Y>
- [57] Q. Deng, C. G. Li, S. L. Wang, H. Tang, H. Zheng, A new method to the treatment of corners in the bem, *Engineering Analysis with Boundary Elements* 37 (1) (2013) 182 – 186. doi:<https://doi.org/10.1016/j.enganabound.2012.03.017>.  
URL <http://www.sciencedirect.com/science/article/pii/S0955799712001439>
- [58] J. R. Rice, Mathematical analysis in the mechanics of fracture, *Fracture: an advanced treatise* 2 (1968) 191–311.
- [59] V. Tomar, J. Zhai, M. Zhou, Bounds for element size in a variable stiffness cohesive finite element model, *International journal for numerical methods in engineering* 61 (11) (2004) 1894–1920.
- [60] B.-L. Wang, Y.-W. Mai, Impermeable crack and permeable crack assumptions, which one is more realistic?, *Journal of applied mechanics* 71 (4) (2004) 575–578.
- [61] H. A. Sosa, Y. Pak, Three-dimensional eigenfunction analysis of a crack in a piezoelectric material, *International Journal of Solids and Structures* 26 (1) (1990) 1 – 15. doi:[https://doi.org/10.1016/0020-7683\(90\)90090-I](https://doi.org/10.1016/0020-7683(90)90090-I).  
URL <http://www.sciencedirect.com/science/article/pii/002076839090090I>
- [62] H. Sosa, On the fracture mechanics of piezoelectric solids, *International Journal of Solids and Structures* 29 (21) (1992) 2613 – 2622. doi:[https://doi.org/10.1016/0020-7683\(92\)90225-I](https://doi.org/10.1016/0020-7683(92)90225-I).  
URL <http://www.sciencedirect.com/science/article/pii/002076839290225I>

- [63] M. L. Dunn, The effects of crack face boundary conditions on the fracture mechanics of piezoelectric solids, *Engineering Fracture Mechanics* 48 (1) (1994) 25 – 39. doi:[https://doi.org/10.1016/0013-7944\(94\)90140-6](https://doi.org/10.1016/0013-7944(94)90140-6).  
URL <http://www.sciencedirect.com/science/article/pii/0013794494901406>
- [64] Y. Shindo, K. Tanaka, F. Narita, Singular stress and electric fields of a piezoelectric ceramic strip with a finite crack under longitudinal shear, *Acta Mechanica* 120 (1) (1997) 31–45. doi:[10.1007/BF01174314](https://doi.org/10.1007/BF01174314).  
URL <https://doi.org/10.1007/BF01174314>
- [65] H. Tian-Hu, S. Zi-Yuan, A new electric boundary condition of electric fracture mechanics and its applications, *Engineering Fracture Mechanics* 47 (6) (1994) 793 – 802. doi:[https://doi.org/10.1016/0013-7944\(94\)90059-0](https://doi.org/10.1016/0013-7944(94)90059-0).  
URL <http://www.sciencedirect.com/science/article/pii/0013794494900590>
- [66] K. P. Herrmann, V. V. Loboda, Fracture-mechanical assessment of electrically permeable interface cracks in piezoelectric bimetals by consideration of various contact zone models, *Archive of Applied Mechanics* 70 (1) (2000) 127–143. doi:[10.1007/s004199900052](https://doi.org/10.1007/s004199900052).  
URL <https://doi.org/10.1007/s004199900052>
- [67] V. Govorukha, V. Loboda, M. Kamlah, On the influence of the electric permeability on an interface crack in a piezoelectric bimaterial compound, *International Journal of Solids and Structures* 43 (7) (2006) 1979 – 1990. doi:<https://doi.org/10.1016/j.ijsolstr.2005.04.009>.  
URL <http://www.sciencedirect.com/science/article/pii/S002076830500226X>
- [68] Y. Liu, Fast multipole boundary element method: theory and applications in engineering, Cambridge university press, 2009.
- [69] M. Bebendorf, Hierarchical matrices: a means to efficiently solve elliptic boundary value problems, Vol. 63, Springer Science & Business Media, 2008.
- [70] I. Benedetti, M. Aliabadi, G. Davi, A fast 3d dual boundary element method based on hierarchical matrices, *International Journal of Solids and Structures* 45 (7?8) (2008) 2355 – 2376. doi:<http://dx.doi.org/10.1016/j.ijsolstr.2007.11.018>.  
URL <http://www.sciencedirect.com/science/article/pii/S0020768307005008>

- [71] I. Benedetti, A. Milazzo, M. H. Aliabadi, A fast dual boundary element method for 3d anisotropic crack problems, *International Journal for Numerical Methods in Engineering* 80 (10) (2009) 1356–1378. doi:10.1002/nme.2666.  
 660 URL <http://dx.doi.org/10.1002/nme.2666>
- [72] T. Olson, M. Avellaneda, Effective dielectric and elastic constants of piezoelectric polycrystals, *Journal of Applied Physics* 71 (9) (1992) 4455–4464. arXiv:<https://doi.org/10.1063/1.350788>, doi:10.1063/1.350788.  
 665 URL <https://doi.org/10.1063/1.350788>
- [73] C.-W. Nan, D. R. Clarke, Piezoelectric moduli of piezoelectric ceramics, *Journal of the American Ceramic Society* 79 (10) (1996) 2563–2566. arXiv:<https://onlinelibrary.wiley.com/doi/pdf/10.1111/j.1151-2916.1996.tb09016.x>, doi:10.1111/j.1151-2916.1996.tb09016.x.  
 670 URL <https://onlinelibrary.wiley.com/doi/abs/10.1111/j.1151-2916.1996.tb09016.x>  
 x
- [74] J. Y. Li, The effective electroelastic moduli of textured piezoelectric polycrystalline aggregates, *Journal of the Mechanics and Physics of Solids* 48 (3) (2000) 529 – 552. doi:[https://doi.org/10.1016/S0022-5096\(99\)00042-3](https://doi.org/10.1016/S0022-5096(99)00042-3).  
 675 URL <http://www.sciencedirect.com/science/article/pii/S0022509699000423>
- [75] A. Fröhlich, A. Brüeckner-Foit, S. Weyer, Effective properties of piezoelectric polycrystals, in: *Smart Structures and Materials 2000: Active Materials: Behavior and Mechanics*, Vol. 3992, International Society for Optics and Photonics, 2000, pp. 279–288. doi:10.1117/12.388212.  
 URL <http://dx.doi.org/10.1117/12.388212>
- [76] L. P. Khoroshun, T. I. Dorodnykh, The effective piezoelectric properties of polycrystals with the trigonal symmetry, *Acta Mechanica* 169 (1) (2004) 203–219. doi:10.1007/s00707-003-0054-1.  
 680 URL <https://doi.org/10.1007/s00707-003-0054-1>
- [77] F. Narita, T. Kobayashi, Y. Shindo, Evaluation of dielectric and piezoelectric behavior of unpoled and poled barium titanate polycrystals with oxygen vacancies using phase field method, *International Journal of Smart and Nano Materials* 7 (4) (2016) 265–275. arXiv:<https://doi.org/10.1007/s00707-003-0054-1>  
 685

[//doi.org/10.1080/19475411.2017.1278834](https://doi.org/10.1080/19475411.2017.1278834), doi:10.1080/19475411.2017.1278834.

URL <https://doi.org/10.1080/19475411.2017.1278834>

- 690 [78] E. Pan, F. Tonon, Three-dimensional green's functions in anisotropic piezoelectric solids, International Journal of Solids and Structures 37 (6) (2000) 943–958.
- [79] G. L. Smith, J. S. Pulskamp, L. M. Sanchez, D. M. Potrepka, R. M. Proie, T. G. Ivanov, R. Q. Rudy, W. D. Nothwang, S. S. Bedair, C. D. Meyer, et al., Pzt-based piezoelectric mems technology, Journal of the American Ceramic Society 95 (6) (2012) 1777–1792.
- 695 [80] V. Gulizzi, A. Milazzo, I. Benedetti, Fundamental solutions for general anisotropic multi-field materials based on spherical harmonics expansions, International Journal of Solids and Structures 100 (2016) 169–186. doi:10.1016/j.ijsolstr.2016.08.014.